J. Fluid Mech. (2009), *vol.* 621, *pp.* 69–102.
doi:10.1017/S0022112008004254 Printed in the United Kingdom

Axially homogeneous, zero mean flow buoyancy-driven turbulence in a vertical pipe

MURALI R. CHOLEMARI[1]
AND JAYWANT H. ARAKERI[2]†

[1]Department of Applied Mechanics, Indian Institute of Technology Delhi, New Delhi 110016, India

[2]Department of Mechanical Engineering, Indian Institute of Science Bangalore 560012, Karnataka, India

(Received 28 July 2007 and in revised form 15 September 2008)

We report an experimental study of a new type of turbulent flow that is driven purely by buoyancy. The flow is due to an unstable density difference, created using brine and water, across the ends of a long (length/diameter = 9) vertical pipe. The Schmidt number Sc is 670, and the Rayleigh number (Ra) based on the density gradient and diameter is about 10^8. Under these conditions the convection is turbulent, and the time-averaged velocity at any point is 'zero'. The Reynolds number based on the Taylor microscale, Re_λ, is about 65. The pipe is long enough for there to be an axially homogeneous region, with a linear density gradient, about 6–7 diameters long in the midlength of the pipe. In the absence of a mean flow and, therefore, mean shear, turbulence is sustained just by buoyancy. The flow can be thus considered to be an axially homogeneous turbulent natural convection driven by a constant (unstable) density gradient. We characterize the flow using flow visualization and particle image velocimetry (PIV). Measurements show that the mean velocities and the Reynolds shear stresses are zero across the cross-section; the root mean squared (r.m.s.) of the vertical velocity is larger than those of the lateral velocities (by about one and half times at the pipe axis). We identify some features of the turbulent flow using velocity correlation maps and the probability density functions of velocities and velocity differences. The flow away from the wall, affected mainly by buoyancy, consists of vertically moving fluid masses continually colliding and interacting, while the flow near the wall appears similar to that in wall-bound shear-free turbulence. The turbulence is anisotropic, with the anisotropy increasing to large values as the wall is approached. A mixing length model with the diameter of the pipe as the length scale predicts well the scalings for velocity fluctuations and the flux. This model implies that the Nusselt number would scale as $Ra^{1/2}Sc^{1/2}$, and the Reynolds number would scale as $Ra^{1/2}Sc^{-1/2}$. The velocity and the flux measurements appear to be consistent with the $Ra^{1/2}$ scaling, although it must be pointed out that the Rayleigh number range was less than 10. The Schmidt number was not varied to check the Sc scaling. The fluxes and the Reynolds numbers obtained in the present configuration are much higher compared to what would be obtained in Rayleigh–Bénard (R–B) convection for similar density differences.

† Email address for correspondence: jaywant@mecheng.iisc.ernet.in

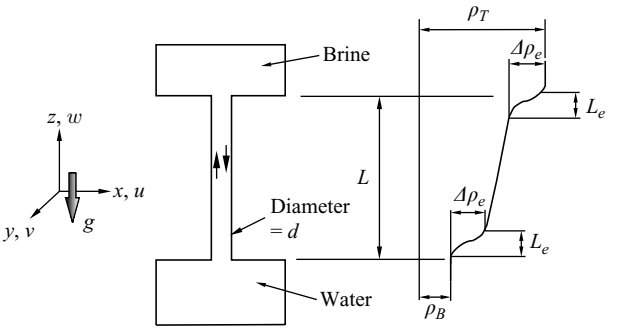

FIGURE 1. Flow schematic. The flow is caused by the density difference ($\rho_T - \rho_B$; $\rho_T > \rho_B$) across the pipe. The tanks have uniformly mixed fluids; there is a developing region near the pipe entrance at each end (L_e, with a density drop of $\Delta\rho_e$), and the density variation in the axially homogeneous midsection is linear.

1. Introduction

Buoyancy is important in many technologically relevant and naturally occurring turbulent flows. In most of these flows, e.g. a plume, both mean shear and density difference are important; turbulence is produced by the interaction of mean shear and the Reynolds shear stresses, and the stratification may aid or impede turbulence production. In this paper we propose and experimentally study a new type of turbulent flow that is purely buoyancy-driven and also homogeneous in the vertical direction.

The flow is created by an unstable density difference across the ends of a long vertical pipe (whose length to diameter ratio L/d is 9; figure 1). We use brine and fresh water for creating the density difference. Mass conservation implies that at any instant of time the net flow is zero at 'any' cross-section of the pipe. Moreover, at high enough Rayleigh numbers, when the flow is turbulent, our experiments show that the time-averaged velocity at any point is zero – with zero mean flow; only fluctuating velocities are present. Since the pipe length-to-diameter ratio is large, the flow away from the ends is 'axially homogeneous' with a linear density gradient.

Thus we have an axially homogeneous turbulent flow with zero mean velocity that is sustained purely by buoyancy. The present work is initiated to obtain a better understanding of buoyancy effects in turbulence by studying it in the absence of shear. The non-dimensional parameters of the flow are the Rayleigh number $Ra = g(1/\rho_0 \Delta\rho/L)d^4/\nu\alpha$, the Schmidt number $Sc = \nu/\alpha$ and the aspect ratio $AR = L/d$. Here $\Delta\rho$ is the density difference across the ends of the pipe; ν is the kinematic viscosity; and α is the diffusivity of the species creating the density difference. The Rayleigh number is based on the mean density gradient $\Delta\rho/L$, and the pipe diameter d. A more appropriate Rayleigh number $Ra_g = g(1/\rho_0 \mathrm{d}\rho/\mathrm{d}z)d^4/\nu\alpha$ in the homogeneous region is based on the local density gradient, $\partial\rho/\partial z$. In our experiments, the Taylor microscale Reynolds number Re_λ is estimated to range from about 45 to 65 (§ 5.1); see table 1. We note that convection driven by a temperature difference instead of a concentration difference would be similar, except the diffusivity of the active scalar would be larger (Prandtl number Pr replacing Sc), but the wall conduction of heat will be an additional parameter.

With a view towards understanding some aspects of ventilation Epstein (1988) experimentally studied the buoyancy-driven exchange (countercurrent) flow through single or multiple openings (both square and circular) in horizontal partitions, using brine above the partition and fresh water below the partition. The openings were

Time (min)	$\Delta\rho/\rho$	$\langle w_{rms}\rangle_A$ (mm s^{-1})	$d\mathscr{L}_{ww}^{L(1/2)}/\langle w_{rms}\rangle_A$ (s)	$\langle flux\rangle_A$ (m^2 s^{-3})	η (mm)	λ (mm)	Nu_g	Ra_g	Re_λ	Re
5	0.0081	10.90	1.33	5.06×10^{-6}	0.38	5.99	4.16×10^5	3.34×10^8	65.3	545
10	0.0065	9.73	1.49	3.59×10^{-6}	0.41	6.34	3.72×10^5	2.66×10^8	61.7	486
20	0.0044	8.03	1.81	2.02×10^{-6}	0.47	6.98	3.07×10^5	1.81×10^8	56.1	402
30	0.0032	6.80	2.13	1.23×10^{-6}	0.54	7.59	2.60×10^5	1.30×10^8	51.6	340
40	0.0024	5.91	2.45	0.81×10^{-6}	0.60	8.14	2.26×10^5	0.98×10^8	48.1	295
50	0.0018	5.16	2.81	0.54×10^{-6}	0.65	8.7	1.97×10^5	0.75×10^8	45.0	258

TABLE 1. Experimental parameters at various times during the experiments; $\langle w_{rms}\rangle_A$ is the average over the measurement area of w_{rms}, 8.6% more than the value at the axis (see figures 4 and 8); $d\mathscr{L}_{ww}^{L(1/2)}/\langle w_{rms}\rangle_A$ is an eddy turnover time; $\mathscr{L}_{ww}^{L(1/2)}$ is from table 2; $flux$ is from (3.3); $\epsilon = g\times\langle flux\rangle_A$; and η and λ follow from ϵ(see § 5.1). $Re_\lambda = \langle w_{rms}\rangle_A\lambda/\nu$, and $Re = \langle w_{rms}\rangle_A d/\nu$.

essentially pipes projecting into the enclosures. The L/d ratios of the pipes were in the range 0.01–10. Four different flow regimes were identified as L/d was increased through this range – an oscillatory regime, a counterflow regime and at the largest L/d ratios, a turbulent regime. The third regime was identified where both turbulent diffusion and counterflow took place in different regions in the pipe. At high L/d ratios the flow could be modelled as turbulent diffusion (after Gardener 1977). It was found that the exchange flow rate was independent of viscosity for all practical purposes, and a universal correlation between L/d and the non-dimensional flux could be proposed.

Arakeri *et al.* (2000) reported preliminary results of the flow under consideration. There the focus was on understanding the nature of the flow. In the experimental study, using flow visualization, they identified various regimes as functions of Rayleigh number. At low Rayleigh numbers the flow is laminar, consisting of two streams with each occupying one half of the cross-section (which is referred to as 'half-and-half' flow); the lighter stream flows up, and the other, the heavier one, flows down, with the line demarcating the two fluids being the diameter of the pipe. As the Rayleigh number is increased, a helical structure is observed, with the up- and down-flowing fluids now forming a double helix. At still higher Rayleigh numbers the flow becomes unsteady but remains laminar. Finally, beyond about $Ra_g = 10^7$, the flow is seen to be turbulent with a range of scales. They measured the average salt concentration in the top tank as a function of time and related the rate of change of the average concentration to the average flux of the salt in the pipe. For the turbulent flow, they proposed a mixing length model with the length scale as the diameter of the pipe. In the turbulent case, the measured flux scaled like $\Delta\rho^{3/2}$ as predicted by the model, which is equivalent to $Nu \sim Ra^{1/2}Sc^{1/2}$. Using scaling arguments, Cholemari & Arakeri (2005) have developed relations for flux, including the end effects. The non-dimensional flux is given by $Nu = Cr(AR)Ra^{1/2}Sc^{1/2}$. Data from Epstein (1988), Cholemari (2004) and Arakeri *et al.* (2000) are used to determine Cr. The end effects are restricted to about a diameter at each end, i.e, $L_e \sim d$ (figure 1), unlike in fully developed pressure-driven pipe flow, where the entrance length is several diameters.

Debacq *et al.* (2001) and Debacq, Hulin & Salin (2003) have reported buoyancy-induced mixing in a long vertical pipe. The experiments consisted of a heavier fluid lying over a lighter fluid in the pipe, which were subsequently allowed to mix.

The mixing process is characterized by the Atwood number $At = (\rho_2 - \rho_1)/(\rho_2 + \rho_1)$ with ρ_1 and ρ_2 being the densities of the light and heavy fluids. For $At > 10^{-4}$ the normalized concentration profiles averaged over the pipe section were seen to be self-similar, allowing the characterization of the phenomenon by a macroscopic diffusion coefficient. The spreading of the front was like $t^{1/2}$. In Debacq *et al.* (2003), the variation of the properties of the flow with the Atwood number ($At = 10^{-5} - 2$), fluid viscosity ($\nu = 1 - 16 \times 10^{-6}$ m^2 s^{-1}) and the pipe diameter (2–24 mm) are studied. An unexpected increase in the diffusivity and characteristic velocity of the random fluid motions results when ν is increased. This results from the coarser mixing of the more viscous fluids, which increases the local density contrasts and thus the buoyancy forces. Although the works of Debacq *et al.* (2001, 2003) and the present work share some common features, there is one fundamental difference. We have an axially homogeneous flow that can be considered quasi-steady, while the flows considered in the studies of Debacq *et al.* are spatially varying and unsteady, more akin to those found in Rayleigh–Taylor instability experiments.

As in the present flow, in Rayleigh–Bénard (R–B) convection, in the bulk, most of the turbulent kinetic energy is produced by buoyancy; the flow is homogeneous (if the convection cell is wide enough and if the mean flow is absent) in the horizontal plane. However, the bottom and top walls play a dominant part in determining the flow (e.g. Siggia 1994; Theerthan & Arakeri 1998, 2000; Stringano & Verzicco 2006), and hence the scaling for the flux could be different in the two cases. In R–B convection, a number of studies (Constantin & Doering 1999; Niemela *et al.* 2001; Amati *et al.* 2005; Nikolaenko *et al.* 2005; Doering, Otto & Reznikoff 2006; Niemela & Sreenivasan 2006, to cite just a few) suggest a $Nu \sim Ra^{1/3}$ scaling, although $Nu \sim Ra^{1/2}$ scaling is predicted in R–B convection at very high Ra (Kraichnan (1962). In particular, the works of Constantin & Doering (1999) and Doering *et al.* (2006) predict a rigorous upper binding to the exponent at 1/3, albeit with a logarithmic correction, when the Prandtl number is infinite. The numerical investigations by Amati *et al.* (2005) ($AR = 2$) and the experimental investigations by Nikolaenko *et al.* (2005) (a range of L/d up to 3.5) and Niemela & Sreenivasan (2006) ($L/d = 4$) of R–B convection in cells with L/d ratios greater than unity also showed a 1/3 scaling of the Rayleigh number. In Amati *et al.* (2005), the exponent was close to 1/3 for four decades of Rayleigh numbers up to 2×10^{14}. In Niemela & Sreenivasan (2006) the exponent saturates close to 1/3 up to 5×10^{12}. A similar saturation of the exponent close to 1/3 occurs for $Ra \sim 10^{12}$ in the study of Nikolaenko *et al.* (2005). In the ongoing work of Verzicco & Sreenivasan (2008) a simulation is carried out for a tall cylindrical cell with $L/d = 10$. The exponent is approximately 0.37 for $Ra \sim 10^{10} - 10^{15}$. However, at the same time, evidence exists that the appearance of such scaling in R–B convection is dependent on the behaviour of the boundary layers near the top and bottom plates. Roche *et al.* (2001) found such a scaling in R–B convection with rough top and bottom plates, beyond Rayleigh number $Ra = 2 \times 10^{12}$, while Niemela *et al.* (2000), with smooth surfaces, did not find the scaling even at much higher Rayleigh numbers close to 10^{17}. Roche *et al.* (2001) argue that this is due to the removing of the Rayleigh number dependence of the boundary layers because of the surface roughness in their experiments. In the experiments of Niemela *et al.* (2000) the near wall dynamics are shear-dominated. Niemela & Sreenivasan (2003) conclude that, in such cases, the observed exponent, close to 1/3, is consistent with Kraichnan's (1662) formula of $Nu \sim Pr^{-1/4} Ra^{1/2}/[(\log Ra)^{3/2}]$; the Pr and the logarithmic terms together yield an effective asymptotic slope of 0.315 over the range of Ra considered. Lohse & Toschi (2003) also found the $Ra^{1/2}$ scaling in their simulations of the bulk turbulence only,

without the bottom and top walls (and therefore without the boundary layers that are present in R–B convection).

In view of such contradictory evidences, it would be useful to study the bulk and the boundary layer effects separately. The present work is an attempt in this direction. The large aspect ratio ensures that any boundary layer effects introduced in the top and bottom tanks do not affect the turbulence in the central region. Further, the boundary layers like ones that occur at the horizontal walls in R–B convection cannot be present in the present experiments. In addition, an important result of the present work is the educing of the structure of turbulence using velocity field measurements with particle image velocimetry (PIV).

Numerical experiments of R–B turbulence with periodic boundary conditions are reported in Calzavarini *et al.* (2005). They thus exclude the boundary layer effects by design. They confirm the scalings given in Grossmann & Lohse (2000) for the bulk of R–B convections. The present measurements and the scalings are shown to be consistent with their theory, supporting the view that the present flow is similar to the bulk turbulence in R–B convection.

Recently, Gibert *et al.* (2006) have reported measurements on convective heat flux and temperature gradient in a vertical channel of aspect ratio 2 (L/b, i.e. channel height to width) filled with water. The data are scaled by a natural length scale L_n, which is based on the mean vertical temperature gradient and the magnitude of the temperature fluctuations. The Nusselt number scales like $Nu \sim \sqrt{Ra_n Pr}$, with the Rayleigh number Ra_n based on L_n which itself has a logarithmic dependence on Re_n, $L_n \sim \log Re_n$. The present configuration has a much larger aspect ratio of 9, thus ensuring a fully developed turbulent flow at the central region. We feel that the small aspect ratio of the apparatus of Gibert *et al.* (2006) could cause the characteristics of turbulence be affected by the flow outside the channel, as will be discussed in § 5.3.

As mentioned above, the absence of a mean flow implies that mean shear is zero. Thus, flow near the wall is shear-free wall-bound turbulence. There have been various studies on shear-free turbulence near a solid wall: Uzkan & Reynolds (1967), Thomas & Hancock (1977), Hunt & Graham (1978), Perot & Moin (1995) and Aronson, Johansson & Löfdahl (1997). In such studies a solid surface is suddenly introduced in homogeneous isotropic turbulence. In the absence of a mean shear, as there is no production, the turbulence decays with time. In the present flow also, the mean shear near the walls (and elsewhere) is zero but with the crucial difference that the turbulence, sustained by buoyancy, is non-decaying. Perot & Moin (1995) studied the decaying turbulence numerically, near an idealized permeable wall, an idealized free surface and a solid wall. In particular they elucidated the role of the pressure–strain correlation near the walls: these transport energy towards the wall when the structures near the wall, called splats and anti-splats in the literature, acquire an imbalance due to viscous effects. They also showed that the spatial extent of wall normal stresses scales with an integral scale, but variation of the tangential stresses is limited to a region that scales with a viscous length scale. Aronson & Löfdahl (1997) experimentally verified the scaling of the spatial extents of the flow near a moving belt. They also showed that the near wall peaks in the measured tangential stresses in Thomas & Hancock (1977) were spurious, thus showing that their results were consistent with those of Perot & Moin (1995), Hunt & Graham (1978) and Uzkan & Reynolds (1967). We will show that the present flow near the walls has some similarities with the shear-free wall-bound turbulence studies, but there are also some differences because of buoyancy. Also, we propose that this flow may be a good way to study non-decaying shear-free turbulence near a wall.

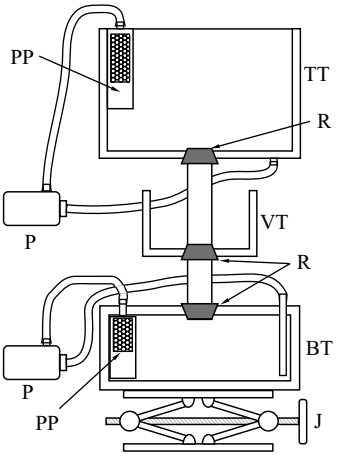

FIGURE 2. Schematic of the experimental setup. Two tanks on either side of a vertical pipe with brine in the top tank and water in the bottom tank create an unstable density gradient which drives the flow. Fluid within each tank is well mixed to provide unambiguous boundary conditions to the pipe. See text for the notation and additional details.

The rest of the paper is organized as follows: We describe the experiments and the diagnostics, confirm the flow is axially homogeneous and give the scalings for the velocities and the fluxes through a model in § 2 . In § 4 we present the characteristics of turbulence through visualizations and velocity statistics. We report the large-scale structure of the flow and indicate the mechanisms of transfer of buoyant energy to turbulence. We discuss the near wall behaviour of the present flow and compare it with that in shear-free wall-bound flows. In discussing these results in § 5, we describe the modes of energy production and transport and discuss the flow in relation to other buoyant flows. Preliminary results of the present study are reported in Arakeri & Cholemari (2002).

2. Experiments

The experimental setup, shown schematically in figure 2, consists of a vertical glass pipe connecting two tanks. The top tank (TT) was open at the top, while the bottom tank (BT) was closed on all sides. The bottom tank was 20 cm $\times$ 20 cm in cross-section and 8 cm high, while the top tank measured 20 cm $\times$ 20 cm $\times$ 20 cm. The tanks were made of glass and perspex. Length of the glass pipe was 450 mm, and its diameter was 50 mm. The tanks were attached at the ends of the pipe by rubber stoppers (R) with holes drilled through them to accommodate the pipe. The ends of the pipe were flush with the tank walls. This design was modular and allowed for different lengths and diameters of the pipes to be accommodated.

Small aquarium water pumps (P) were used to continuously mix the fluids and thus prevent stratification in each tank. The uniformly mixed conditions in the tanks ensured known and unambiguous boundary conditions at the pipe ends. The locations of the two exits (through perforated pipes PP) and the two inlets of the pumps were arranged along opposite diagonals of the tank, well away from the pipe exit. In addition, the flow rates in the pumps of about 8 litres per minute were small enough, so as to minimize the disturbance levels near the pipe ends. For clarity only part of the mixing circuit is shown in the figure.

To minimize effects of refraction, all the visualizations and PIV measurements are done through a square glass tank (VT) filled with water and enclosing the pipe. The side of this tank nearest to the camera is perpendicular to the mean line of sight and parallel to the laser sheet.

The general procedure in the experiments was as follows: The brine was prepared using common salt (NaCl) weighed using a balance with the least count of 1 mg. We filled the bottom tank and the pipe with distilled water. After sealing the top opening of the pipe with a stopper, we filled the top tank with brine whose volume equalled the total volume of water in the pipe and the bottom tank. For PIV measurements, both the brine and the distilled water were seeded with particles (hollow glass spheres from Potters Industries Inc., 110P8, with a mean diameter of 11 μm and mean density 1.1 g cc^{-1}). We ensured that there were no air bubbles in the pipes leading to the pumps or anywhere else in the setup. A plumb line was used to ensure that the pipe was vertical.

Each experiment was started by removing the stopper. Typically, the initial salt concentration in the top tank was 0.01 g cc^{-1}. About 5 min were required for the initial transients to die out and the flow to be established. The salt concentration in the top tank reduced with time and that in the bottom tank increased with time. At the end of the experiment the densities of the fluids in the two tanks were nearly equal. The experiments typically lasted about 3 hours, but we consider the data till about 50 min after the start of the experiment, when the flow was well within the turbulent regime.

We measured the salt concentration in the top tank using a conductivity probe (ORION SENSORLINK, model PCM100). The accuracy of measurement was better than 13 $mg\,l^{-1}$. We acquired the data averaged over every 40 s. Knowing the time rate of variation of the salt concentration in the top tank and using an integral mass balance, we can calculate the concentration difference and the flux of the salt as functions of time. Note that, from continuity considerations and incompressibility assumption, at any instant of time the axial velocity averaged over the cross-section of the pipe

$$\int_A \tilde{w}\,\mathrm{d}A = 0, \tag{2.1}$$

where $\tilde{w}$ is the velocity in the vertically upward and z the direction; see figure 1 for the coordinate system notation. The tilde represents the total velocity (mean + fluctuating). This relation holds for both laminar and turbulent flows; for turbulent flows, as we shall see below, the time-averaged velocity at any point is also zero.

In the following, we denote the top and bottom tank concentrations by C_T and C_B respectively. V_T, V_B and V_P refer to the volumes of the top and bottom tanks and the pipe, respectively; A_P is the cross-sectional area of the pipe; M_S is the total mass of the salt in the setup; and F is the flux of salt through the pipe. From mass conservation of salt we have

$$C_B(t) = \frac{M_S - C_T(t)(V_T + V_P/2)}{V_P/2 + V_B}, \tag{2.2}$$

$$\Delta C(t) = C_T - C_B = \frac{C_T(t)(V_T + V_B + V_P) - M_S}{V_P/2 + V_B}, \tag{2.3}$$

$$\langle F \rangle_A A_P = \rho_0 V_T \mathrm{d}C_T/\mathrm{d}t. \tag{2.4}$$

Thus from the measurement of top tank concentration with time, we can determine the instantaneous concentration difference between the top tank and the bottom tank

fluids as well as the area-averaged salt flux $\langle F \rangle_A$. Salt concentration is related to density by

$$\frac{\partial \rho}{\partial C} = \rho_0 \beta, \tag{2.5}$$

where ρ_0 is the density of water, and $\beta \approx 0.7$ for the salt concentration range encountered in the experiments. Thus, the density difference between the top and the bottom tanks is

$$\Delta\rho = \rho_0 \beta \Delta C. \tag{2.6}$$

We obtained velocity statistics in a plane passing through the pipe axis using PIV. The measurement area was 50 mm $\times$ 50 mm and approximately halfway along the pipe. The images were obtained with an interline transfer CCD PIV camera (IDT Technologies) set to 1024^2 px resolution, at 8 bits, and using an 120 mJ Nd-YaG pulsed laser (Quantel Big Sky Laser). The interrogation windows had a size of 32^2 px, and the spatial resolution was 1.6 mm (0.8 mm with 50% overlapping windows). The Kolmogorov length scale η is estimated in § 5.1 as 0.4 mm or larger, with an average of approximately 0.5 mm (see table 1). Hence the spatial resolution was 4η or better. We estimate the r.m.s. errors to be better than 0.3 mm s^{-1} or less. Two hundred and twenty data sets consisting of 250 frames, each recorded a second apart, from 19 different experiments were obtained. The duration of each data set corresponds to about 125 eddy turnover times. (A mean value of 2 s is taken for the eddy turnover time; see table 1.) Each frame had 63^2 vectors. In all the cases, the particle image diameter was close to 2 px, which is recommended to minimize the overall error of uncertainty (Raffel, Willert & Kompenhans 1998; Prasad 2000). The details of the image evaluation and error analysis are in Appendix A.

2.1. *Axial homogeneity*

Since the pipe is long, the flow is expected to be axially homogeneous or fully developed away from the ends of the pipe, with the statistics of the flow, and in particular the various averages, having no dependence on z, the axial coordinate. An analogous axially homogeneous situation is obtained in a fully developed pressure-driven pipe flow, where the flow is driven by a linear pressure gradient. In the present case, the convection is driven by a linear density gradient; the detailed arguments for the existence of a linear density profile are given in Appendix B. We measured the average concentration profile along the length of the pipe, by means of an absorption technique. Figure 3 shows that the concentration variation is fairly linear in the range measured, i.e. about two diameters from either end. Due to experimental constraints we could not measure the concentration profiles till the ends of the pipe. However, in the present flow, the developmental region at either end is short, about one diameter, much smaller compared to the case of pressure-driven pipe flow (Cholemari & Arakeri 2005).

3. Scaling

For a long enough pipe ($L/\mathrm{d} \gg 1$), away from the two ends the flow must be homogeneous in the axial direction with a linear density gradient. Also, the local large length scale for a long enough pipe is the pipe's diameter. We present further evidence of this in § 4.3. The mixing length model (Arakeri *et al.* 2000) is based on the dominance of the pipe diameter as the single length scale (also see § 4.3.1). In the fully developed region, the only relevant parameters are the pipe diameter d, the

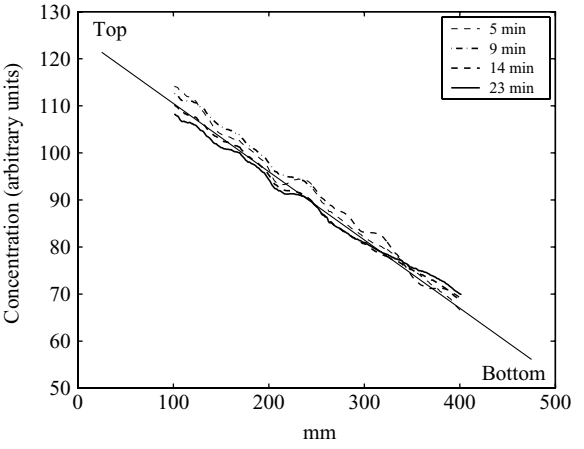

FIGURE 3. Mean concentration gradient measured using absorption (pipe $AR = 10$). Data averaged for about 2 min. The decrease of the gradient with time is seen. The straight line is drawn for comparison.

axial gradient of the mean density $\mathrm{d}\rho/\mathrm{d}z$, g, ν and α. The two molecular diffusivities are not expected to be relevant for the scalings of the energy containing scales. Then dimensional analysis gives d as the length scale and the scales for density fluctuations (ρ'), velocity fluctuations (w') and buoyancy flux ρ_m, w_m and F_m/ρ_0 respectively as (with β being defined by $\beta\rho_0\Delta C = \Delta\rho$)

$$\rho' \sim (\mathrm{d}\rho/\mathrm{d}z)d = \rho_m, \tag{3.1}$$

$$w' \sim \sqrt{g(\mathrm{d}\rho/\mathrm{d}z)d^2} = w_m, \tag{3.2}$$

$$\langle flux\rangle_A = \beta\langle\langle wc\rangle\rangle_A \sim \frac{w_m\rho_m}{\rho_0} \sim \frac{F_m}{\rho_0}. \tag{3.3}$$

Physically these relations imply that a fluid particle (a coherent region of fluid) heavier than the surrounding fluid by an amount ρ' attains a 'free fall' velocity w_m as it falls through the mixing length $\simeq d$, before it interacts and mixes. The implicit assumption is that the flow becomes decorrelated over distances scaling with d. Over a height of one diameter ρ' scales with the mean density. Alternatively, if density fluctuations and the density gradient is known, a length scale can be derived as $\rho'/(\mathrm{d}\rho/\mathrm{d}z)$.

The mixing length scalings for velocity are tested in figure 4. PIV data are compared with the mixing length velocity scaling obtained from the salt concentration measurements. The r.m.s. velocities measured on the pipe axis are considered. From salt concentration measurements (2.3), ΔC is evaluated, and then (3.2) and (3.6) are used to evaluate w_m. The fit is good till about 50 min from the start of the experiment, confirming the validity of the scalings for the Rayleigh numbers considered. The scalings, with different constants, work well almost right up to the wall.

These scalings imply that, the Nusselt number $Nu_g = -\langle flux\rangle_A/(\alpha\beta\mathrm{d}C/\mathrm{d}z)$, a non-dimensional measure of the flux (where α is the diffusivity of the salt), scales like

$$Nu_g = C_m Ra_g^{1/2} Sc^{1/2}, \tag{3.4}$$

where $C_m = 0.88$ is the proportionality constant in (3.3), i.e. $\langle flux\rangle_A = C_m F_m/\rho_0$, and is independent of the geometry (Cholemari & Arakeri 2005). The mean concentration

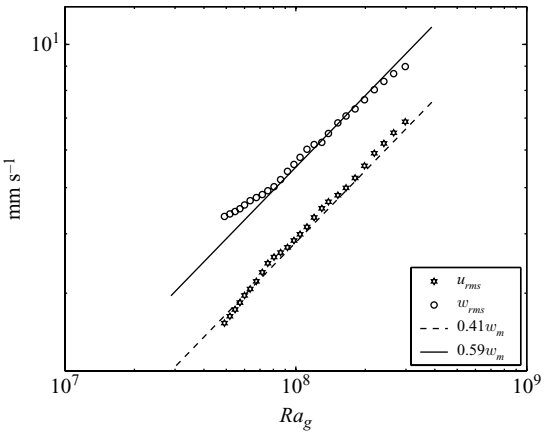

FIGURE 4. The mixing length velocity scaling w_m is compared with the r.m.s. velocities measured at the axis using PIV; w_m is evaluated from salt concentration measurements (2.3), using (3.2). The lines have a slope of 1/2. The scaling is not valid for $Ra_g \leqslant \sim 7.5 \times 10^7$.

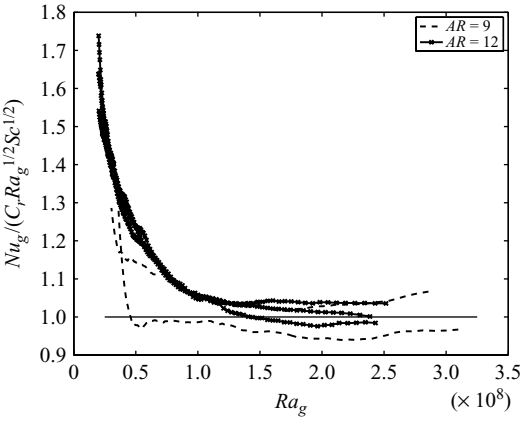

FIGURE 5. The Nusselt number scaling (3.4) is tested against experimental data. The scaling is not valid for $Ra_g \leqslant \sim 1 \times 10^8$.

gradient is denoted by $\mathrm{d}C/\mathrm{d}z$. The Reynolds number $\langle w_{rms} \rangle_A d/\nu$ scales as

$$Re = K_1 Ra_g^{1/2} Sc^{-1/2}, \tag{3.5}$$

where $K_1 = \langle w_{rms} \rangle_A / w_m$ and equals 0.78; $\langle w_{rms} \rangle_A$ is the area average of w_{rms} over the pipe c s^{-1}. At the pipe axis itself, $w_{rms}/w_m = 0.72$ (see figure 4). These relations are analogous to the exact relations for R–B convection given in Chandrasekhar (1981) and Grossmann & Lohse (2000) and can also be derived similarly from integral balances over a volume for the present flow (Cholemari 2004). The velocity scaling is verified in figure 4, and the Nusselt number scaling is verified in figure 5. In the range of Rayleigh numbers available in the present experiment, the measurements support the scalings. However, we note that measurements over a larger range of Rayleigh numbers are required to confirm these scalings. Also the Schmidt number needs to be varied to test its influence as well.

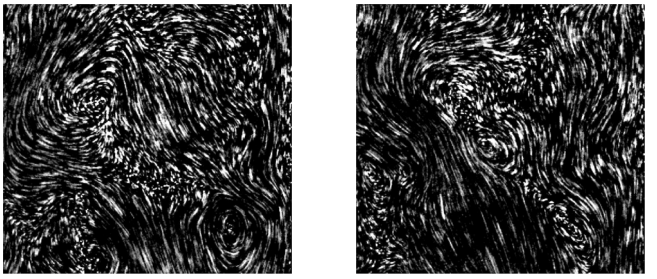

(*a*) (*b*)

FIGURE 6. Particle streak visualization; $Ra_g \sim 2.5 \times 10^8$. The images are 2 s apart. The images show the volume 50 mm × 50 mm × 1.4 mm from the middle of the pipe and symmetric about the pipe axis (vertical in the images). The length of a streak is proportional to the magnitude of velocity in the plane of the light sheet. Note the persistence of the diagonally aligned dumb-bell-shaped structure in the two images.

Because of the nonlinear change in density near the ends, $\mathrm{d}\rho/\mathrm{d}z \neq \Delta\rho/L$. Then

$$\frac{\mathrm{d}\rho}{\mathrm{d}z} = K\frac{\Delta\rho}{L}, \tag{3.6}$$

where K depends on the aspect ratio AR ($\mathrm{K} = 1/(1 + 4.2/AR)$ (Cholemari 2004; Cholemari & Arakeri 2005). For $AR = 9$ in the present experiments, $\mathrm{K} = 0.68$. The Nusselt number based on the overall density difference and the Reynolds numbers scale with the Rayleigh number $Ra = (g(\Delta\rho/L)d^4)/\rho\nu\alpha$ in the following manner:

$$Nu = -\frac{\langle flux\rangle_A}{\alpha\beta\Delta C/L} = C_m K^{-3/2} Ra^{1/2} Sc^{1/2}; \tag{3.7}$$

$$Re = \frac{\langle w_{rms}\rangle_A d}{\nu} = K_1 K^{-1/2} Ra^{1/2} Sc^{-1/2}. \tag{3.8}$$

The prefactors in (3.7) and (3.8) are derived in Cholemari & Arakeri (2005).

4. Characterization of the turbulence

4.1. *Visualization*

Several important features of the flow were revealed by flow visualizations, some apparent from the still pictures and some only after viewing the video: there is no mean flow (figure 6); the flow field appears random and three-dimensional with a range of scales and a range of velocities (figures 6 and 7*a*); characteristic of the turbulent flows, vortical type structures seem to dominate (figures 6 and 7*a*).

Flow visualization reveals a continuous falling of parcels of heavier fluid and rising of parcels of lighter fluid; this is the mechanism by which potential energy is converted to kinetic energy, initially associated with the vertical component of velocity. Collisions and interactions of the downward and upward moving parcels result in lateral velocities.

The particle streak images taken 2 s apart (figure 6) show another aspect of this flow, the persistence of the features for long times at the large scales. For example the dumb-bell-shaped double vortex approximately aligned at 45° to the pipe axis in figure 6(*a*) is still identifiable in figure 6(*b*), although many changes have taken place at the smaller scales. Two seconds corresponds to approximately one and half eddy turnover times at this Rayleigh number.

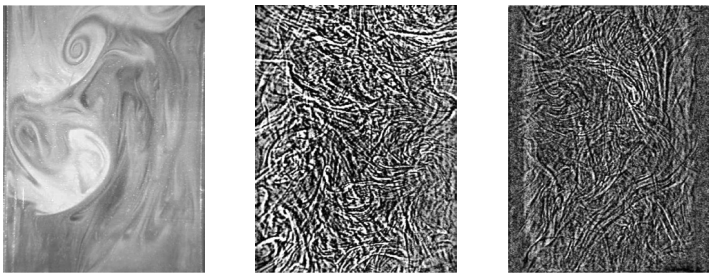

(*a*) (*b*) (*c*)

FIGURE 7. (*a*) Dye visualization; $Ra_g \simeq 1 \times 10^8$. The image corresponds to the volume 50 mm × 67 mm × 1.4 mm from the middle of the pipe, symmetric about the pipe axis (vertical in the image). The image shows a range of scales, the largest being comparable to the pipe diameter, and a range of concentrations – made apparent by the large variation in the brightness. The buoyancy forcing is random and over a range of scales. (*b*), (*c*) Shadowgraphs at $Ra_g \sim 4 \times 10^8$ and $Ra_g \sim 1 \times 10^8$. The same length of pipe as in (*a*) is shown. The flow appears random. Note the decrease in the contrast due to the weaker density fluctuations in (*c*).

In figure 7(*a*), a small amount of sodium fluorescein dye mixed in the top tank fluid at the beginning of the visualization subsequently 'tags' the denser top tank fluid. The regions of higher concentrations of dye appear brighter. Apart from the diffusive effects at the small scales, the dye concentration is proportional to the salt concentration and hence is directly related to the buoyancy force which is responsible for sustaining the turbulence. Clearly the forcing is random and occurs over a range of scales. The up- and down-moving fluids often collide, creating local shears, instabilities and mixing.

In the shadowgraphs (figures 7*b* and 7*c*), the flow structure appears random with no preferred orientation. During the early stages of the experiment, the structure appears granular, while at the later stages, the contrast, due to the reduced density fluctuations, is lower, and the structure is more like randomly interwoven filaments. The fine-grained structure seen in the shadowgraphs is slightly misleading, since the shadowgraph is an integrated effect of light refractions through the test section; the fine-scale structures are not as closely spaced as they appear. The integrating effect of the shadowgraphs averages out lateral variations (which are clearly present in figures 6 and 7*a*) and helps show the absence of axial variation, as expected from axial homogeneity.

The absence of a mean flow appears to be a robust characteristic of the flow; we could not induce the flow to prefer a half–half configuration even when the pipe was tilted by a relatively large angle of about 5° to the vertical. The flow near (about one diameter) the pipe ends is quite different from that in the middle. The average flow across the cross-section near the pipe ends is again zero, but the counterflows are well defined. The flow into the tank (top or bottom) is in the form of a jet and into the pipe is like a sink flow drawing fluid from everywhere in the tank.

4.2. *The mean characteristics of the flow*

The focus of the present study is turbulent convection in the absence of shear. Buoyancy is the only source of energy for the turbulence because the mean shear is zero. (The walls do not participate in shear production; the role of the walls in the flow appears to be similar to that in shear-free flows.) The dynamics of the flow away from the walls are mainly determined by buoyancy. These flow characteristics

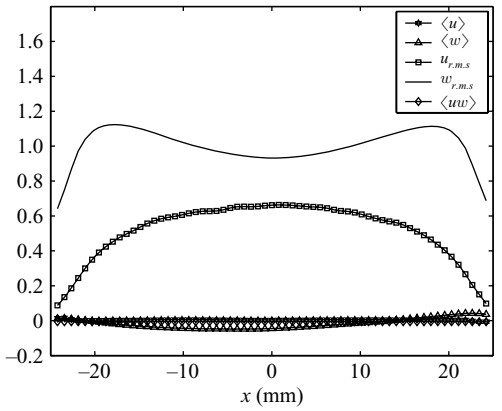

FIGURE 8. Profiles of the mean and the RMS velocities across the pipe cross section. Also shown are the turbulent shear stress $\langle uw \rangle$ and the mean velocities $\langle u \rangle$ and $\langle w \rangle$, which are all nearly zero in the present flow. All velocities are scaled by w_{rms} averaged over the cross-section $\langle w_{rms} \rangle_A$.

and other features of the flow are described in this section, mainly through velocity statistics.

Figure 8 gives the profiles of the mean and r.m.s. velocities. The data is taken after the initial transients have died out while the convection is turbulent. The velocities are scaled by the r.m.s. value of the axial velocity averaged over the domain of the PIV measurement during each 5 min interval. The r.m.s. velocities scale as $\sqrt{g(\mathrm{d}\rho/\mathrm{d}z)d^2}$ (see figure 4 and (3.2)).

Mean flow and the turbulent shear stresses are absent; $\langle u \rangle$, $\langle w \rangle$ and $\langle wu \rangle$ are nearly zero. Only the fluctuating velocities are present, and the r.m.s. velocities are about two decades larger compared to the mean velocities. The absence of shear stresses and a mean flow imply that there is no shear production of turbulence. The average value of the buoyancy production term, calculated from the flux of salt, is about two orders larger than the average-value shear production.

The average value over the cross-section of the lateral component, u_{rms}, is about half of w_{rms}, the axial component, which has a double peak, whereas u_{rms} has a flat maximum at the axis. The natures of the profiles are determined by a combination of effects due to buoyancy and the wall. In shear-free flows, the wall normal component of the velocity is affected to about 1–2 integral length scales, while the axial velocity profile is affected to a much shorter viscous length scale, scaling like $\sqrt{\nu\tau}$, where $\tau = \mathscr{L}_{ww}^{L(1/2)}/w_{rms}$. The present flow near the walls shows similar trends, except that the flow is affected by buoyancy as well. The peaks near the walls in the axial r.m.s. profile are absent in the studies of shear-free flows. It is a speculation whether these are due to the nondecaying nature of the turbulence or due to higher buoyancy production in these regions. Obtaining buoyancy production from the simultaneous measurement of the density and velocity would resolve this issue. However, the flow in the central region is dominated by buoyancy.

Both the presence of the walls and buoyancy cause anisotropy in the present flow. One of the indicators of anisotropy at the large scales are the ratios of the r.m.s. velocities in different directions. Figure 9 shows the ratio $\langle w^2 \rangle / \langle u^2 \rangle$. A broad minimum of about 2 exists at the centre of the pipe. As the wall is approached, the ratio rises to very large values that are around 50. The axial velocities diminish due to viscous

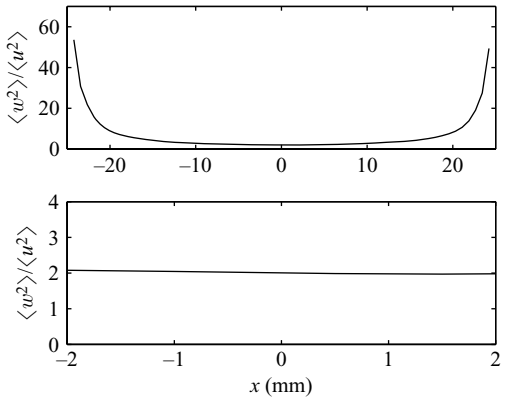

FIGURE 9. Variation of the large-scale anisotropies of the flow across the pipe cross-section. Large-scale anisotropy is characterized by the ratio of the mean square velocities $\langle w^2\rangle/\langle u^2\rangle$.

effects as the wall is approached, while the lateral velocities diminish due to kinematic blocking. As the wall is approached, the reduction in lateral velocity is over a larger spatial extent (integral scale) compared to the spatial extent over which reduction in the axial velocity occurs. The difference in these length scales results in the large anisotropies as the wall is approached (also see figure 8).

We may compare the values of the ratios of the normal stresses obtained in some buoyancy-driven turbulent flows, with those in the present flow. In R–B convection, in the bulk, $\langle w^2\rangle/\langle u^2\rangle \approx 1.3$ (Fitzjarrald 1976). In a statistically homogeneous turbulence created by homogeneous random fluctuations of density in an unbound, uniform fluid with zero mean gradient of density $\langle w^2\rangle/\langle u^2\rangle \approx 2.8$ or 2.4, depending on the initial density profile (Batchelor, Canuto & Chasnov 1991). For the vertical, buoyant turbulent boundary layer the ratio is about 2 at the location of peak production of k and about 2.3 midway towards the wall from this location. In the present flow, $\langle w^2\rangle/\langle u^2\rangle \approx 2$ near the centre, rising steeply to large values near the walls (figure 9).

The result that the Reynold's shear stress is zero is also seen in figure 10, which shows that the scaled joint probability density function (JPDF) is nearly circular and is symmetric about the ordinate (with u/u_{rms} and w/w_{rms} nearly independent and $\langle wu\rangle/(u_{rms}w_{rms}) \approx 0$; Tennekes & Lumley 1972). The entire data, i.e. data for the duration of the experiment considered and for the full lateral extent, has been taken to calculate the JPDF.

4.3. *Large-scale structure of the flow*

Next we present the spatial structure of the flow and estimate the large length and time scales of the present flow, using velocity correlation functions. In the present flow, for separations in the axial direction (the homogeneous direction), the spatial velocity correlation function does not depend on the coordinate but just on the separation, $\boldsymbol{r}$. Similarly, temporal correlations calculated over spans of a few minutes do not depend on time t but only on the temporal separation τ; the flow may be assumed to be stationary over the time in which the change in the driving density difference is negligible. As in case of the velocity profiles, the velocities are scaled by the average r.m.s. value of the axial velocity during each 5 min interval (a 'data set'), before ensemble averaging.

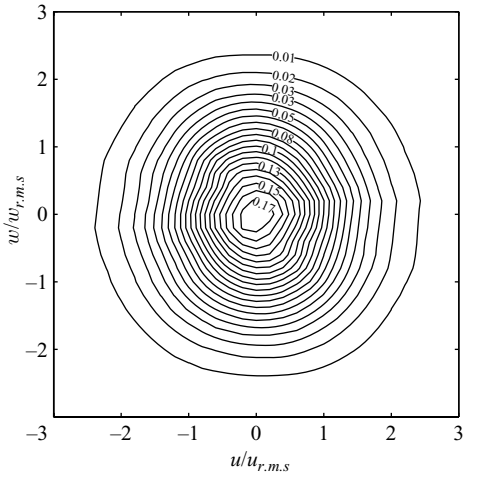

FIGURE 10. Joint PDF of the velocities, scaled by their r.m.s. values. The symmetry about the ordinate indicates $\langle wu \rangle \simeq 0$.

4.3.1. *Spatial correlation*

The velocity spatial correlation is defined as

$$C^{S}_{u_i u_j}(\boldsymbol{x}_0, \boldsymbol{r}, t) = \frac{\langle \langle u_i(\boldsymbol{x}_0, t) u_j(\boldsymbol{x}_0 + \boldsymbol{r}, t) \rangle_n \rangle_t}{u_{ir.m.s.}(\boldsymbol{x}_0, t) u_{jr.m.s.}(\boldsymbol{x}_0 + \boldsymbol{r}, t)}. \tag{4.1}$$

The superscript S indicates a spatial correlation; $\boldsymbol{x}_0$ is the reference point; and $\boldsymbol{r}$ is the separation vector. The subscripts n and t indicate the average taken over different data sets and over time in each set respectively. The r.m.s. values are given by

$$u_{ir.m.s.}(\boldsymbol{x}, t) = \left(\langle \langle u_i(\boldsymbol{x}, t)^2 \rangle_n \rangle_t \right)^{1/2}. \tag{4.2}$$

The spatial velocity correlations are shown in figure 11 for three choices of the reference point, $x_0 = -22.4$ mm, $x_0 = -12.5$ mm and $x_0 = 0$ mm, and with $z_0 = 0$, for all the three cases. The walls are about 0.8 mm away on either edge of the correlation maps. The top row shows the lateral velocity maps, while the bottom row shows the axial velocity maps.

The axial velocity correlation maps are stretched in the vertical direction, with distinct negative correlation regions on either side. These features suggest that parcels of fluids moving vertically are elongated in the axial direction; dictated by continuity, a downward- or upward-moving parcel is accompanied by parcels moving in the opposite direction on the sides. The correlation maps give a quantitative scale to the lumps of heavier or lighter fluid moving down or up observed in laser-induced flourescence (LIF) visualization. With the reference point on the axis of the pipe ($x = 0$), the lateral velocity correlation maps are nearly circular in the central region, with no clear regions of negative correlation.

As the reference point is moved closer to the wall, first to $x = -12.5$ mm (halfway between the pipe axis and the wall) and then to $x = -22.5$ mm, the velocity correlation maps get increasingly affected by the presence of the wall. At $x = -12.5$ mm, the shape of axial velocity correlation maps do not change significantly, but the lateral velocity maps begin to get squashed near the walls. Close to the wall ($x = -22.5$ mm) both the maps exhibit significant changes in their structure. All the axial velocity correlation maps show distinct negative correlation regions, suggesting counterflow.

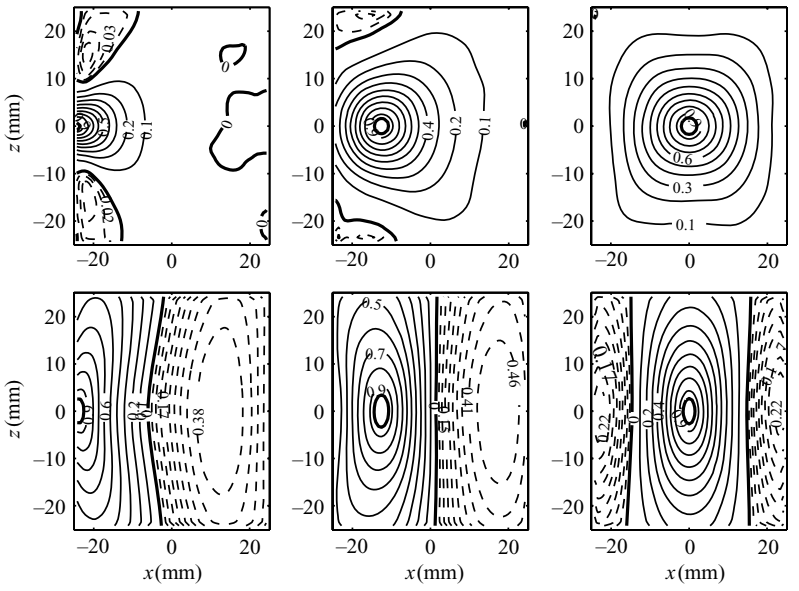

FIGURE 11. Velocity correlations. The origins are at −22.4, −12.5 and 0 mm from the pipe axis and at $z = 0$. Top row: lateral velocity. Bottom row: axial velocity. Full lines correspond to positive correlation, and dashed lines correspond to negative correlation.

The effect of the wall on the wall normal velocity extends further away from the wall than in the case of the axial velocity. This is also seen in the decay of the lateral velocity fluctuations over a larger distance compared to the decay length for the axial velocity fluctuations (figure 8). As we shall discuss in § 5, in the present flow, the energy is fed only into the vertical velocity fluctuations by gravity. The energy gets transferred to the lateral velocity components by the action of the pressure–velocity correlations, which are isotropic away from the walls. The correlation maps reflect this difference, with the stretched axial velocity maps and the nearly circular lateral velocity maps.

In all cases, extent of the correlations, an indication of the large-scale structures, is comparable to the pipe diameter.

Integral length scales $\mathscr{L}$, for example

$$\mathscr{L}^{L}_{uu} = \int_{-\infty}^{\infty} C^{S}_{uu}(x, r_x)\mathrm{d}r_x, \tag{4.3}$$

are usually used to obtain the large scales of turbulence. Since the flow is non-isotropic, we have four integral scales, longitudinal and transverse, corresponding to the two velocity components – $\mathscr{L}^{L}_{uu}$, $\mathscr{L}^{T}_{uu}$, $\mathscr{L}^{L}_{ww}$ and $\mathscr{L}^{T}_{ww}$, where the superscripts L and T represent longitudinal and transverse respectively. The integral length scale defined above is useful if the correlation goes to zero in the measured area. In the present flow, with a limitation on the area of measurement, the correlation did not always go down to zero, and thus, alternately we define correlation lengths to represent the large scales which are defined as the length at which the correlation function drops down to a certain value, say 0.5. These we denote $\mathscr{L}^{T(1/2)}_{uu}$ and the like by $\mathscr{L}^{L(1/2)}_{uu}$.

Figure 12 gives the variation in the lateral direction of the correlation lengths $\mathscr{L}^{L(1/2)}_{ww}$ and $\mathscr{L}^{T(1/2)}_{uu}$, normalized with the pipe diameter d. The average is over all data sets. The correlation length for the axial velocity, $\mathscr{L}^{L(1/2)}_{ww}$, has a peak at about 6 mm

	$\mathscr{L}^{L}_{ww}$, $\mathscr{L}^{L(1/2)}_{ww}$	$\mathscr{L}^{T}_{ww}$, $\mathscr{L}^{T(1/2)}_{ww}$	$\mathscr{L}^{L}_{uu}$, $\mathscr{L}^{L(1/2)}_{uu}$	$\mathscr{L}^{T}_{uu}$, $\mathscr{L}^{T(1/2)}_{uu}$
Correlation length	0.29	0.14	0.20	0.17
Integral scale	0.33	0.14	0.22	0.19

TABLE 2. The large scales of turbulence on the pipe axis calculated from the velocity correlations. The scales are normalized by the pipe diameter.

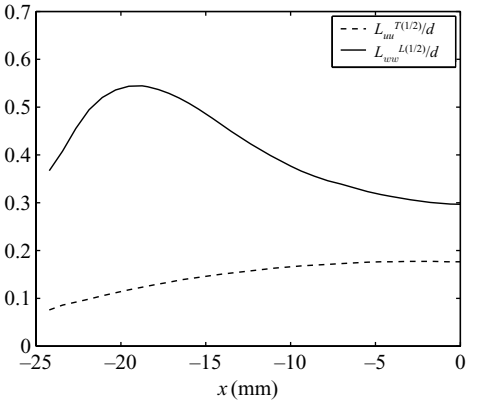

FIGURE 12. Variation of correlation lengths, normalized with the pipe diameter, with lateral distance; −25 mm corresponds to the wall and the pipe axis is at 0 mm.

($\sim d/8$) from the wall, close to the location at which the peak of the axial velocity fluctuation also occurs (figure 8). There is a smooth increase in $\mathscr{L}^{T(1/2)}_{uu}$ from near the wall to the maximum at the centre. The wall appears to act as a guide to the axial velocity component, increasing the extent of the axial velocity correlation, while the lateral velocity fluctuations are attenuated by the wall, decreasing the axial extent of the correlation as the walls are approached. These features are seen in the correlation maps (figure 11). There is not much variation in the correlation lengths for different values of Rayleigh number.

Table 2 gives the summary of large scales of the present flow, calculated on the axis. The large scales are seen to be comparable to the pipe diameter. It is seen that the longitudinal correlation lengths in the axial direction $\mathscr{L}^{L(1/2)}_{ww}$ is larger by a factor of about two compared to the other three correlation lengths ($\mathscr{L}^{T(1/2)}_{ww}$, $\mathscr{L}^{L(1/2)}_{uu}$ and $\mathscr{L}^{T(1/2)}_{uu}$), which are all of similar magnitudes. The integral scales have similar magnitude as the respective correlation lengths.

The temporal correlations of velocity exhibit persisting correlations over long times, typically over 10 s (about 5 eddy turnover times) or so. The long-term correlation is related to the persistence of large structures, as seen in the streak images (figure 6). The persistence of the temporal correlations at long times implies that the number of truly independent data sets reduce as time of separation increases. Thus the statistics at the large scales involving larger velocities would be relatively noisier. The relation between Eulerian spatial and temporal velocity correlations is further explored in Cholemari (2004) and Cholemari & Arakeri (2006). Note that the standard Taylor's hypothesis, used to relate temporal statistics to spatial statistics, is not valid in the absence of a mean flow.

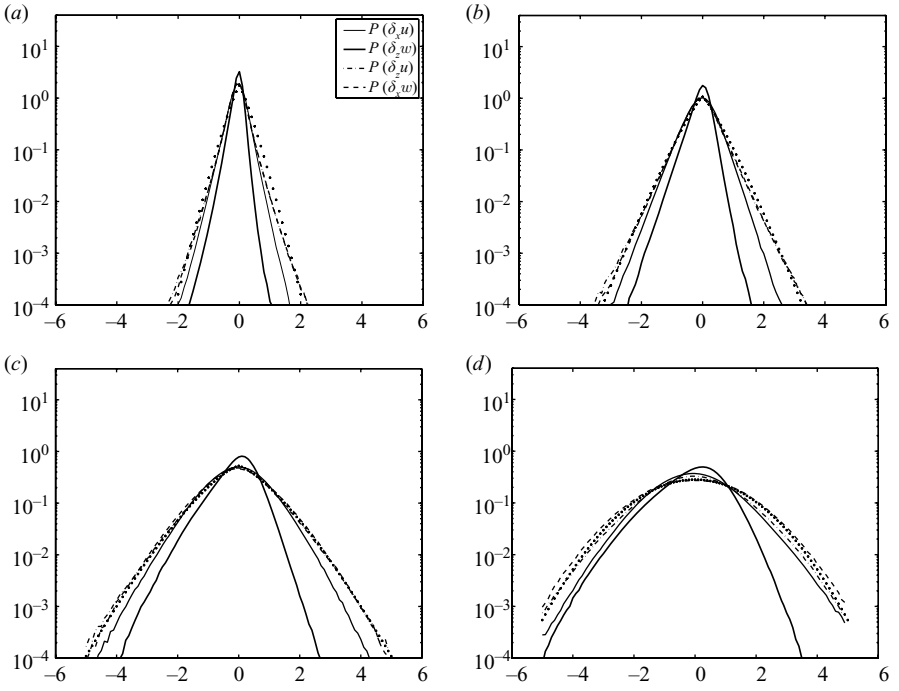

FIGURE 13. The PDFs of reduced velocity differences, at various separations. Data is from the mid two-thirds of the pipe cross-section. The stretched exponentials $e^{-\alpha|\zeta|^\beta}$ are indicated by dots. The pipe diameter $d \sim 125\eta$. (*a*) $\delta x, z/\eta = 4$; dots-$(1/0.5747)e^{-4.1|\zeta|^{1.18}}$; (*b*) $\delta x, z/\eta = 8$; dots-$(1/0.9347)e^{-2.3|\zeta|^{1.18}}$; (*c*) $\delta x, z/\eta = 20$; dots-$(1/1.9022)e^{-0.95|\zeta|^{1.36}}$; (*d*) $\delta x, z/\eta = 40$; dots-$(1/3.5437)e^{-0.25|\zeta|^2}$.

4.4. *Indications of energy transfer processes and the wall effects*

From the correlation maps in § 4.3.1 we have identified one type of fluid motion to be of elongated masses of fluid moving up or down. The probability density functions (PDFs) of velocity differences and cross-correlation maps of velocities indicate another type of fluid motion, consisting of collisions of coherent regions of fluid. We hypothesize that the main mechanism of energy transfer from the axial to the lateral direction in the central region is through collision of these fluid masses. We will also see how the dynamics of the flow in the central region of the pipe differ with that near the walls.

For making comparisons, we consider the wall-affected region as about a sixth of the pipe cross-section from the wall (see figures 8 and 9). In this region there is about 80% of the variation in lateral normal stress ($\langle uu \rangle$) and a larger variation in the axial normal stress ($\langle ww \rangle$). Statistics from this region will be compared with those from the central region.

The PDFs of the reduced velocity differences, e.g. $\delta_x u/u_{rms}$, in the central region are given in figure 13. Here, $\delta_x u = u(x + \Delta x, z, t) - u(x, z, t)$ and $u_{rms} = \langle \langle \sqrt{\langle (u(x, z, t))^2 \rangle_t} \rangle_z \rangle_x$. For these plots, the averaging for u_{rms} and w_{rms} is from the selected region. The PDFs $\delta_x u$ and $\delta_x w$ are for lateral separations, while the PDFs $\delta_z u$ and $\delta_z w$ are for axial separations. The separations $\delta z/\eta$ (or $\delta x/\eta$) of 4, 8, 20 and 40 (corresponding to $0.032d$, $0.064d$, $0.16d$ and $0.32d$, respectively) are considered. Here η is the Kolmogorov length scale, $(\nu^3/\epsilon)^{1/4}$, and is estimated by equating the

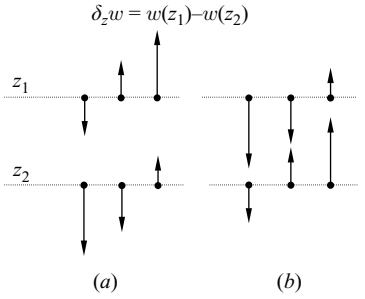

FIGURE 14. Schematic of the (*a*) separation ($\delta_z w > 0$) and (*b*) collision ($\delta_z w < 0$) events, where $\delta_z w = w(z_1) - w(z_2)$ with $z_1 > z_2$; w is positive upward.

dissipation ϵ to the production $\mathscr{P}$, which can be calculated from the measured mass flux of salt. The smallest value of η, about 0.4 mm, occurs at the beginning of the experiment, and it steadily increases thereafter, due to the reduction in the flux. The average value during an experiment is about 0.5 mm. However, the separations are given in terms of the initial value of 0.4 mm. To increase the sample size, homogeneity in the axial direction and symmetry about the midplane are assumed. Unless otherwise mentioned, two columns at the desired distance are used to calculate the PDFs for the x differences; the number of data points is $250 \times 220 \times 2 \times 63$. Similarly in the case of velocity differences in the z direction, two rows at the desired separation and extending five unit distances either side of the central axis are used to calculate the PDFs; the number of data points is $250 \times 220 \times 2 \times 11$.

In figure 13(*a*), corresponding to the smallest separation, the PDFs of $\delta_z w$ and $\delta_x u$ are asymmetrical, the former being markedly so; $\delta_z w$ or $\delta_x u < 0$ corresponds to fluid particles approaching each other, and $\delta_z w$ or $\delta_x u > 0$ corresponds to fluid particles moving apart. The two 'cross' PDFs, $\delta_x w$ and $\delta_z u$, are (as expected) symmetrical and nearly equal, and a stretched exponential with unit area can be fitted (dots). In the present flow $Re_\lambda \sim 45 - 65$ is sufficiently high, such that the buoyancy forcing effects at the large scales are not felt at the small scales, and for some statistics at least, the flow has universal characteristics at the small scales. Noullez *et al.* (1997) found in a turbulent jet, at separations of few η, the PDFs follow stretched exponentials. As the separation is increased to twice this value (figure 13*b*), the PDF of $\delta_z w$ (thick line) separates even more from the rest, which are still approximated by a stretched exponential. At separation of $\delta/\eta = 20$, (figure 13*c*), the two 'cross' PDFs have become Gaussian; i.e. the exponent is 2, and with a standard deviation of 1.1; the asymmetry in the PDF of $\delta_z w$ is even more pronounced, but the asymmetry in the PDF of $\delta_x u$ has reduced. The asymmetry in the PDF of $\delta_z w$ continues to a separation of $\delta/\eta = 40$ ($= 0.32d$), (figure 13*d*) and then reduces, but the asymmetry in the PDF of $\delta_x u$ reverses. At this separation, the two lateral PDFs follow a Gaussian curve with a standard deviation of $\sqrt{2}$, $(1/\sqrt{4\pi})\mathrm{e}^{-\zeta^2/4}$ as is expected at large separations (Noullez *et al.* 1997). As the separation is increased beyond the respective correlation regions (see figure 11 and table 2) first the PDF of $\delta_x u$ and then $\delta_z w$ approach the Gaussian distribution.

The remarkable feature of the PDFs of the velocity differences is the pronounced asymmetry of the PDFs for $\delta_z w$ and to a lesser extent for $\delta_x u$. To understand these asymmetries, figure 14 schematically shows the interaction of two fluid particles, along the z-axis, for example, located at z_1 and z_2, Δz apart. When $\delta_z w < 0$, the relative motion between particles is towards each other, (figure 14), while $\delta_z w > 0$ indicates

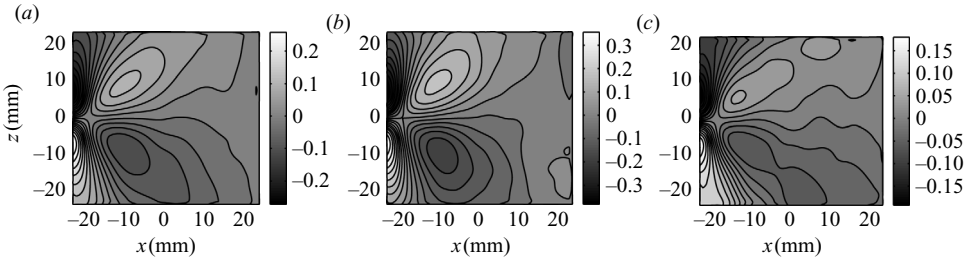

FIGURE 15. Cross correlation maps near the wall, $\langle u(x_0, z_0)w(x, z)\rangle / u_{rms}(x_0, z_0)w_{rms}(x, z)$. In ($a$) all the data is considered; in (b) the data in which $u(x_0, z_0)$ is towards left, i.e. towards the wall, are considered; while in (c) data correspond to $u(x_0, z_0)$ towards right. Forty-one per cent of the events contribute to (b), while 59% contribute to (c).

a relative motion away from each other (figure 14b). The asymmetry in the PDFs of $\delta_z w$ indicates that $\delta_z w < 0$ occurs more frequently than $\delta_z w > 0$. It is also seen in figure 13 that the largest relative velocities are obtained for the $\delta_z w < 0$ (collision) events than the $\delta_z w > 0$ (separation) events. This asymmetry is because of the fluid particles continually approaching and colliding with each other. This also explains the reversing of the asymmetry PDF of $\delta_x u$ at larger separations; collisions of vertically moving fluid parcels in the central region will squeeze the fluid laterally, and there is relative separation in the lateral direction at large distances. But at smaller δ_x, collision events take place. However, the number of $\delta_x u$ collision events is smaller when compared with $\delta_z w$ collision events, as seen by the smaller asymmetry in the PDFs of $\delta_x u$. The considerable reduction in the asymmetry in the PDF of $\delta_z w$ (not shown) beyond the separation of $\delta/\eta = 60 (\simeq 0.5d)$ indicates the size of the particles involved in the collisions: somewhat more than half the pipe diameter ($d \simeq 125\eta$ or less).

To summarize the observations with respect to the central zone, the PDFs of the velocities, in particular, the asymmetry in those of $\delta_z w$ indicate collisions of vertically moving fluid particles. Correlation maps suggest elongated regions, scaling with the pipe diameter, of up- and down-moving fluids, creating a local counterflow on the sides. We suggest that the collisions of vertically moving fluid parcels, indicated by the asymmetry of the PDFs of velocity differences, is the mechanism of energy transfer from vertical to lateral directions.

4.4.1. *Wall effects*

The kinematic blocking affects the wall normal velocity component, and its effect is felt over an integral length scale. In contrast, viscous effects affect the tangential velocity near the wall. To understand the near wall flow, we look at the cross-correlation maps with the reference point near the wall. Consider the cross-correlation maps near the wall (figure 15), with the origin at 2.3 mm from the left wall. In figure 15(a) all data are considered, while figure 15(b) corresponds to cases in which the fluid at the reference location moves left (towards the wall), and in figure 15(c) the fluid at the reference point moves right (away from the wall), i.e. $u(x_0, z_0)$, negative or positive. A motion towards the wall (a splat event) is associated with flow away from the point of impingement along the wall. The lateral velocity correlation maps near the wall ($\boldsymbol{x}_0 = -22.4$ mm), as seen in figure 11, where the presence of two negatively correlated regions indicates flow away from the wall some z distance away from the reference point. For motion away from the wall (an anti-splat event) the flow picture would be similar except that all the flow directions would be reversed.

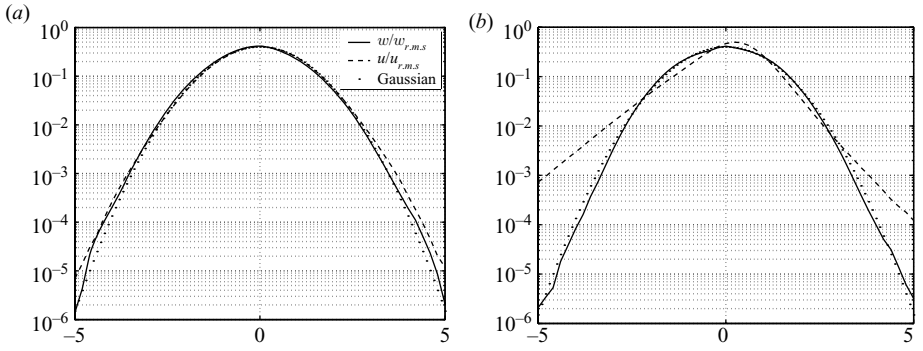

FIGURE 16. The PDFs of the velocities: (*a*) data only from the middle third of the pipe; (*b*) data from near the left wall of the pipe, covering a span of $d/6$. The reference Gaussian curve, $(1/\sqrt{2\pi})\mathrm{e}^{-\zeta^2/2}$, is indicated by dots.

Cross-correlation maps in the central region have a diagonal symmetry, suggesting displacement ahead and behind moving fluid parcels.

Although the correlation maps in the three cases are roughly similar, the number of events contributing to the left (towards the wall) or right (away from the wall) are 41% and 59% respectively. Idealizing the anti-splat event to occur axisymmetrically about the location of the splat event, we would observe the anti-splat at two locations in the plane of the laser sheet, for every splat event. Hence, near a wall, the condition on u would divide the data approximately in the ratio 1:2, the majority being away from the wall. The magnitude of the correlation is correspondingly less in figure 15(*c*) when compared to figure 15(*b*). In case of the displacement events in the central zone, the ratio is close to 1:1. The ratio gradually decreases from close to 2:1 near the wall to 1:1 at the axis.

The wall influences the PDFs of velocities and velocity differences. Figure 16(*a*) shows the PDFs of lateral and axial velocities, normalized with their respective r.m.s. velocities, for example $\sqrt{\langle (u(x,z,t))^2 \rangle_t}$. The data is taken from the middle third of the pipe. A reference Gaussian curve with unit variance is shown by dots in the figure. Noullez *et al.* (1997) found a similar behaviour for spatially resolved measurements in a turbulent round jet ($Re_\lambda \approx 360 - 600$). However, when the data from near the wall, covering a distance of $d/6$, are considered, because of the kinematic blocking effects, the tails of the PDFs of the lateral velocity depart sharply from the Gaussian (figure 16*b*). The asymmetry in the PDF is due to the difference in the wall-approaching and wall-leaving fluids. The PDFs of the axial velocity in this wall region, however, still remain Gaussian.

Figure 17 shows the PDFs of velocity differences in the lateral and axial directions at a separation $\delta/\eta = 8$ from regions close to the wall. Figure 17(*a*) is for lateral separations, at a mean distance of 2.3 mm ($\simeq 12\eta$, $= 3/64d$) from the wall. The wall normal component has a slightly asymmetrical PDF, while the axial PDF is symmetrical (as expected) and narrower. Figure 17(*b*) is for axial separations, at a mean distance of 2.3 mm ($\simeq 12\eta$, $= 3/64d$) from the wall. The axial velocity PDF shows no marked asymmetry, indicating the collision and separation events are equally likely. Further, the wall normal component shows relatively stronger differences when compared to those of wall tangential component, as might be expected from the kinematic blocking effects of the wall. In figure 17(*c*), at a distance of 7.8 mm ($\simeq 40\eta$, $= 10/64d$) from the wall, the PDFs of $\delta_z w$ have begun to become asymmetrical, indicating the beginning of regions in which buoyancy is important. A

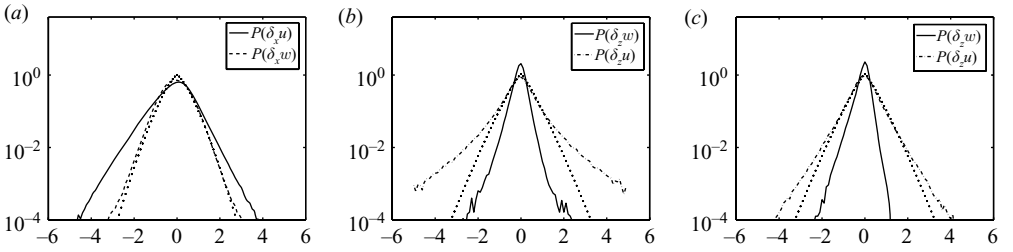

FIGURE 17. The PDFs of velocity differences from near the wall: (*a*) and (*b*) are for a mean distance of 2.3 mm from the wall, while (*c*) is for a mean distance of 8 mm from the wall. Compare with figure 13(*b*). The wall normal component shows significant deviations. The PDF of $\delta_z w$ is symmetrical in (*b*) but begins to become asymmetrical in (*c*). (*a*) $\delta x/\eta = 8$; dots-$(1/0.5747)\mathrm{e}^{-4.1|\zeta|^{1.18}}$; (*b*) $\delta z/\eta = 8$; dots-$(1/0.9347)\mathrm{e}^{-2.3|\zeta|^{1.18}}$; (*c*) $\delta z/\eta = 8$; dots-$(1/0.9347)\mathrm{e}^{-2.3|\zeta|^{1.18}}$.

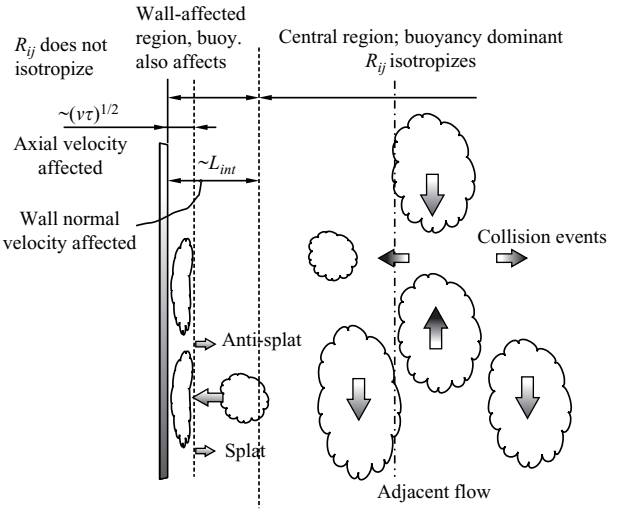

FIGURE 18. Schematic of the phenomenology of processes occurring in the flow. The flow consists of two distinct regions: a central region in which most of buoyant energy is converted into kinetic energy in the axial direction and subsequently to energy in the horizontal directions, mainly through collisions of fluid particles, and a near wall region similar to that in shear-free wall-bound turbulent flows.

further difference is in the PDFs of $\delta_z u$: these show large deviations from the stretched exponential in figure 17(*b*), while in figure 17(*c*) these are quite close to the stretched exponential; the kinematic wall-blocking effects on the wall normal component have reduced. In the central region, (figure 13*b*) a stretched exponential fits the PDFs of $\delta_z u$ quite well. The data points $250 \times 220 \times 2 \times 5$ were used to calculate the PDFs in figures 17(*b*) and 17(*c*).

From the cross-correlation maps of the velocities and the PDFs of velocity differences, we infer the presence of two distinct regions in the flow: a near wall region similar to that in shear-free wall-bound flows and a central region in which most of the buoyant energy is converted to energy in the vertical direction and collisions of fluid particles subsequently produce lateral motions. In some region near the wall kinematic-blocking effects of both the wall and buoyancy are present. Figure 18 summarizes the main processes and interactions.

As in the earlier studies of shear-free turbulent flows (Perot & Moin 1995; Aronson & Löfdahl 1997), the wall normal Reynolds stress is affected to an integral length scale ($\sim d$), whereas for the wall tangential Reynolds stresses the relevant length scale is a viscous length scale $\sqrt{\nu\tau}$, where $\tau = \mathscr{L}_{ww}^{L(1/2)}/\langle w_{rms}\rangle_A$ is the eddy turnover time (table 1).

The wall normal component has no significant variation beyond about 15 mm ($\sim d/3$) from the wall, which is about $\mathscr{L}_{ww}^{L(1/2)}$; in case of shear-free wall-bound flows it is about twice the integral scale. In case of wall tangential velocity, since τ has a mean value of about 2 s for the first 50 min of the experiment, the viscous length scale turns out to be 1.4 mm, while from figure 8, the region till the peak in the w_{rms} profile appears to be about 7.5 mm, about $5.3\sqrt{\nu\tau}$. This can be compared with the value of about $4\sqrt{\nu\tau}$ in the study of Perot & Moin (1995), although there is a small dependence on the Reynolds number. The main difference in the present flow as compared to shear-free wall-bound flows is that of the buoyant energy being converted into lateral fluctuations in regions away from the wall through collisions of axially moving fluid particles.

5. Discussion

The vertical acceleration of the fluid due to buoyancy and the collisions which produce the lateral components are the main features of the energy transfer processes in the present flow. We now look at some of these in more detail and, in this context, compare some other turbulent flows with the present flow.

5.1. *Energetics*

Stationarity, axial homogeneity and absence of mean flow and mean shear considerably simplify the equations governing the convection. The advection terms in the equation for kinetic energy $k = u_i u_i/2$, $(\overline{D}/\overline{D}t)k$, are zero in the present problem. The shear production of turbulence $\langle u_i u_j\rangle \partial_i U_j$ is absent, as the shear stresses $\langle u_i u_j\rangle$ as well as the mean shear $\partial_i U_j$ are zero. The production is just because of buoyancy. The turbulent kinetic energy balance (e.g. Pope (2000) becomes

$$\partial_i \mathscr{T}_i = \mathscr{P} - \epsilon, \tag{5.1}$$

where $\partial_i \mathscr{T}_i$ denotes the turbulent transport terms; $\mathscr{P} = -g_i\beta\langle u_i c\rangle = -g\beta\langle wc\rangle$ is the production; and ϵ is the viscous dissipation of the turbulent kinetic energy. Since the flow is axially homogeneous, there is balance between production and dissipation in each cross-section; the transport terms just redistribute the kinetic energy in the cross-sectional plane. By taking an average over the cross-section the equation becomes

$$\langle \mathscr{P}\rangle_A = \langle \epsilon\rangle_A; \tag{5.2}$$

i.e. the average production in each cross-sectional plane is exactly balanced by the average dissipation in that plane. This result is useful for estimating the dissipation ϵ from the measured mass flux of salt. This enables us to estimate the Kolmogorov microscale η and the Taylor microscale λ as

$$\left.\begin{aligned} \eta &= (\nu^3/\epsilon)^{1/4}, \\ \lambda &= \left(15\nu\langle w_{rms}\rangle_A^2/\epsilon\right)^{1/2}, \end{aligned}\right\} \tag{5.3}$$

from which we estimate the Taylor-microscale-based Reynolds number $Re_\lambda = \langle w_{rms}\rangle_A \lambda/\nu$.

The equation for the Reynolds stresses is (Pope 2000);

$$\partial_k(T_{kij}) = \mathscr{P}_{ij} + \mathscr{R}_{ij} - \epsilon_{ij}; \tag{5.4}$$

the transport term on the left side of the equation balances the production of the stresses $\mathscr{P}_{ij}$, the redistribution due to pressure fluctuations $\mathscr{R}_{ij}$ and the dissipation ϵ_{ij}, on the right. The production is only due to buoyancy:

$$\mathscr{P}_{ij} = \beta(g_i\langle u_j c\rangle + g_j\langle u_i c\rangle). \tag{5.5}$$

Effect of the redistributive term is to isotropize the flow, in the central region, by transferring energy from the axial to the lateral components through the collision events, but near the wall, due to the imbalance in the structures, the energy transport is in the reverse, from the lateral to the axial components, similar to the case of shear-free wall-bound flows (Perot & Moin 1995).

The area-averaged equations for the normal stresses are given by

$$-2\beta g\langle\langle wc\rangle\rangle_A + 2\langle\langle p'/\rho\partial_z w\rangle\rangle_A = \langle\epsilon_{ww}\rangle_A, \tag{5.6}$$

$$2\langle\langle p'/\rho\partial_x u\rangle\rangle_A = \langle\epsilon_{uu}\rangle_A, \tag{5.7}$$

$$2\langle\langle p'/\rho\partial_y v\rangle\rangle_A = \langle\epsilon_{vv}\rangle_A. \tag{5.8}$$

The first equation shows that buoyancy production directly feeds into the axial component of energy which is either dissipated or redistributed into the other two components through the pressure velocity correlations. As $\langle p'/\rho\partial_i u_i\rangle = 0$ from continuity, (5.6)–(5.8) show that $\langle p'/\rho\partial_z w\rangle$ is a sink term for the vertical component $\langle ww\rangle$ of the energy and forms source terms for the lateral components $\langle uu\rangle$ and $\langle vv\rangle$. A similar situation occurs in pressure-driven fully developed pipe flows; turbulent kinetic energy is produced by shear production in the axial direction, which is redistributed in the lateral direction (Monin & Yaglom 1971). Since the pressure velocity correlations have an isotropizing effect, the lateral velocity components are more isotropic than the axial velocity component, in the region away from the walls as seen in figure 11. The sum of (5.6)–(5.8) gives (5.2), the area-averaged kinetic energy equation.

Analogous to relations for R–B convection given in Chandrasekhar (1981), Siggia (1994) and Grossmann & Lohse (2000), exact relations can be obtained between Nusselt number and the dissipation of kinetic energy and between Nusselt number and the dissipation of scalar variance for the present flow (Cholemari (2004). These are

$$\alpha K^2 Nu_g(\frac{\Delta C}{L})^2 = \langle\epsilon_c\rangle_V \tag{5.9}$$

and

$$\frac{\nu^3}{d^4}(Nu_g - 1)Ra_g Sc^{-2} = \langle\epsilon\rangle_V. \tag{5.10}$$

Estimating the dissipation rates using the mixing length scales in (5.10) as gF_m/ρ_0, we get

$$Nu_g - 1 = C_m Ra_g^{1/2} Sc^{1/2}. \tag{5.11}$$

Neglecting 1 when compared to the large value of Nu_g, we recover (3.4). From this we conclude that the mixing length scalings are consistent with the assumption of the dissipation and production balance on an average, across the pipe (also see (5.2)).

The dissipative scale of the scalar fluctuations is also indicated by (5.9). Estimating the dissipative scalar fluctuations to have a magnitude of $\beta\rho_m$ and taking their scale

to be ℓ,

$$\ell \sim \frac{d}{\sqrt{Nu_g}} \sim d\left(C_m^2 Ra_g Sc\right)^{-1/4}. \tag{5.12}$$

For the present configuration, at 20 min, for example (see table 1), $\ell \sim 90$ μm. For comparison, the Batchelor scale $\sim \eta/\sqrt{Sc}$ is approximately 18 μm. However, the scale of scalar fluctuations at which the buoyancy effects manifest scales with d (3.1).

In all the above relations, Prandtl number (Pr) will replace Sc in the case of convection caused by temperature difference.

5.2. *Comparison with fully developed pipe flow*

As opposed to the present flow in which the turbulence is sustained only by buoyancy production shear flows have shear production as the only source of energy for turbulence. In the wall-bound shear flows like fully developed pipe flows both the effects of the wall – the kinematic blocking as well as shear – are present. One common feature between the fully developed pipe flow and fully developed pipe convection is axial homogeneity. The former is driven by a constant pressure gradient, and the turbulence is sustained by shear; the latter is driven by a constant density gradient, and the turbulence is sustained by buoyancy. The wall plays a dominant role in pressure-driven pipe flow, where almost all the production of turbulent kinetic energy is near the walls at which most of it is also dissipated. The rest of the turbulent kinetic energy is transferred to the region away from the wall by turbulent diffusion. A similarity with the pressure-driven pipe flow with pipe convection is that turbulence production is only in the axial component of kinetic energy. The other two components obtain the kinetic energy through the redistribution term. The direct numerical simulation (DNS) study of two-dimensional channel flow of Kim, Moin & Moser (1987) (in which $Re = 13750$) gives at $y^+ = 11.8$ the location of the peak production $\langle u^2\rangle/\langle v^2\rangle \sim 42.5$ and at $y^+ = 98$, in the log law region, $\langle u^2\rangle/\langle v^2\rangle \sim 2.6$, while at the centreline, $y^+ = 395$, $\langle u^2\rangle/\langle v^2\rangle \sim 1.47$. Here u is the axial velocity, and v is the wall normal velocity. In comparison the ratio on the centreline in pipe convection is about 2.4 and increases to about 50 near the walls.

5.3. *Comparison with R–B-type of convective flows*

In R–B convection, as in the pipe convection, the production is mainly in the bulk, but the dissipation is mainly near the walls. However, the crucial difference between R–B convection and the pipe convection is the presence of the boundary layers near the walls in R–B convection, which offer a large resistance to the heat transport. On the other hand, in the pipe convection the open ends (where no boundary layers are present) account for much-reduced end resistance. Lohse & Toschi (2003) simulated R–B convection in infinitely tall cavities with constant density gradient, i.e. without the boundary layers. They too observed the $Nu \sim Ra^{1/2}$ scaling. Thus the appearance of $Ra^{1/2}$ scaling appears to depend on the absence of the horizontal boundary layers, or at least, on the boundary layers being independent of Rayleigh number effects. The observations in the present flow as well as the proposed scalings based on the diameter as the length scale are consistent with this view.

Vertical pipe convection has end regions with nonlinear gradients, which are estimated to be about one diameter at each end (Cholemari 2004; Cholemari & Arakeri 2005). Flow at these locations is developing and is still under the influence of the exterior flow. (The largest eddy is in contact with the outer flow.) Thus in the apparatus of Gibert *et al.* (2006), a fully developed flow is unlikely to develop. Some evidence for this is seen in figure 2 of their paper. It is possible that the logarithmic

dependence of L is caused by this scenario, where the scales of the flow within the channel are likely to be affected by the flow outside the channel. And it might also be necessary to use the temperature gradient and the magnitude of the temperature fluctuations to derive a length scale.

In the present experiments, the pipe is sufficiently long to have a fully developed flow (evident in figure 3) with a linear density gradient. Hence we believe the scaling arguments given in § 3 are more appropriate for this flow. Further, note that the density differences across the pipe are produced in bulk across the tanks containing well-mixed fluids (no boundary layers in the tanks).

6. Summary and conclusion

We have studied a turbulent flow in a long vertical tube that is axially homogeneous, and sustained purely by buoyancy. There is no mean flow and thus no mean shear, and hence shear production of turbulence is absent. The flow is driven by a linear unstable density gradient, much like the fully developed pipe flow that is driven by a linear pressure gradient.

Experiments are consistent with a Nusselt number scaling of $Nu_g \sim Ra_g^{1/2} Sc^{1/2}$, implying a flux independent of molecular diffusivity and viscosity, and a Reynolds number scaling of $Re \sim Ra_g^{1/2} Sc^{-1/2}$. The flux and the velocity scales are predicted by a mixing length model. Experiments covering a large range in Ra are required to confirm the scaling and obtain the precise value of the exponent. Also it is required to vary the Schmidt (or Prandtl) number to obtain its influence on the Nu and Re scaling.

In the present study we have separated the bulk and the boundary layer effects in a turbulent convection, by eliminating the boundary layers. The bulk mechanisms cause the $Nu \sim Ra^{1/2}$ scaling. In the classical R–B convection, the interplay of the bulk and the boundary layer results in the $Nu \sim Ra^{1/3}$ scaling. We conjecture that this is brought about by whichever mechanism is less effective in transporting of the scalar (the 'bottleneck'). If the bulk mechanism is the bottleneck or if the boundary layers do not exist, then the $Nu \sim Ra^{1/2}$ scaling appears. If the boundary layers are the bottleneck, then the $Nu \sim Ra^{1/3}$ scaling prevails.

The convection essentially consists of rising and falling parcels of fluid continually interacting amongst themselves and with the wall. The flow may be divided into three regions (see figure 18). In the central zone the convection is essentially driven by buoyancy. In a region covering about a sixth of the diameter from the wall, the flow is affected both by buoyancy and, as in the case of shear-free wall-bound turbulence, by kinematic blocking of the wall. The third region is the thin viscosity-affected region in which the dissipation of turbulent kinetic energy may be large.

In the central zone, the large-scale motions scale with the pipe diameter. Spatial correlations of axial velocity show extended regions in the vertical direction (figure 11). There seem to be two dominant types of motion. One, indicated by velocity correlation maps, is of the heavier parcels of fluid going down accompanied by lighter parcels of fluid rising up on the sides, while the other, indicated by the PDFs of velocity differences, is collision of vertically moving fluid parcels. In the near wall region, the flow consists of 'splat' and 'anti-splat' events conjectured earlier (Perot & Moin 1995). The production is solely by buoyancy in all regions. Near the axis of the pipe, the ratio $\langle w^2 \rangle / \langle u^2 \rangle$ involving the vertical and lateral velocities (w and u respectively) is about 2. Near the walls, due to wall-blocking effects this ratio is much larger. The velocity PDFs are Gaussian in the central zone.

Some possible extensions of the present work are that, first, simultaneous measurements of the velocity field and scalar field would give a direct measurement of the turbulent flux $\langle wc \rangle$ term which is also directly proportional to the buoyancy production term. These measurements could lead to better models for effects of buoyancy on turbulence. DNS studies of the present turbulent flow with its axially homogeneous region would complement the understanding gained from the experiments. Experiments with a higher Re_λ would enable us to test the scalings over a wider range of parameters.

We believe the features of axial homogeneity or full development, no mean flow and thus turbulent production just by buoyancy, and the $Nu \sim Ra^{1/2}Sc^{1/2}$ scaling makes this flow useful for fundamental studies of buoyancy-driven turbulence. The absence of the bottom and top walls makes the crucial difference between pipe convection and R–B convection; the top and bottom walls (and the associated boundary layers) offer most of the resistance to heat flux. This resistance is removed in pipe convection. In particular, much higher fluxes and Reynolds numbers are obtained in the present flow than in R–B for the same driving density difference.

The authors thank Professor K. R. Sreenivasan for his valuable advice on the manuscript.

Appendix A. Velocity measurement

Two configurations were used to evaluate the PIV process: in the first, set a, the area imaged was a 50 mm $\times$ 50 mm region at the centre of the pipe, while in the second (set b) the area imaged was reduced to half the earlier value. Two hundred and twenty-two data sets consisting of 250 frames, each recorded a second apart, from 19 different experiments were obtained in set a, while the corresponding numbers were 96, 250 and 8 for set b. The images were interrogated with windows of size 32^2 px, yielding a spatial resolution of 4η and 2η for sets a and b respectively. Each frame had 63^2 vectors. In all the cases, the particle image diameter was close to 2 px, which is recommended to minimize the overall error of uncertainty (Raffel *et al.* 1998; Prasad 2000). The analysis in this paper was just with the set a data, with the zoomed data being used only for the validation of the process.

The PIV images were evaluated in two stages, first with a coarse grid with 64^2 windows and then in a fine grid with 32^2 windows. In this stage, one or more passes were done with incremental window offset equal to the local average displacement, till the evaluated displacement was less than 1 px. This approach minimized the measurement uncertainty as well as improved the detectability of the correlation peak by increasing the number of particle matches (Keane & Adrian 1992; Westerweel 1997; Westerweel, Dabiri & Gharib 1997; Raffel *et al.* 1998; Prasad 2000). Using Gaussian sub-pixel estimator to estimate the displacements to within a pixel minimized the peak-locking errors. We also corrected any remaining peak locking by using a model for the error (Cholemari 2007). We minimized the errors arising due to out-of-plane motion of particles aliased as in-plane motions, the so-called perspective errors, by imaging the flow from as far away as possible (2 m in set a and 1.5 m in set b). We tested the algorithm by using synthetic rotation and translation of experimental images and using an image sequence of a particle pattern moved through known distances using a traverse, as well as with the standard images provided by the Japanese Visualization Society (JVS). In the first two cases, the average r.m.s. uncertainty was less than 0.05 px. With the JVS images with particles of 5 px diameter (the smallest provided), the

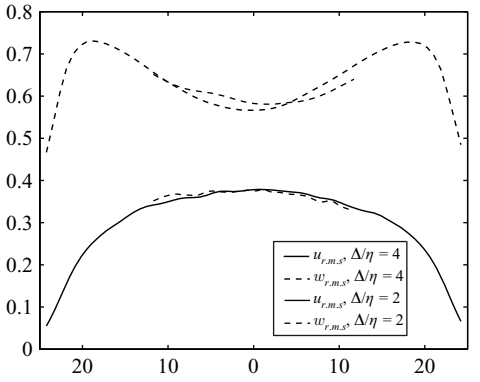

FIGURE 19. Comparison of r.m.s. velocity profiles obtained from set a (resolution $\Delta\eta = 4$) and set b (resolution $\Delta\eta = 2$) experiments. The data from the zoomed experiments are yet to converge at the large scales.

r.m.s. uncertainty was 0.15 px, which compares favourably with the reported value of 0.3 px in Raffel *et al.* (1998). The reported value of r.m.s. uncertainty for particles of 2 px diameter is 0.07 px in Raffel *et al.* (1998), and hence we estimate the error to be at most about 0.05 px in our case. An r.m.s. uncertainty of 0.05 px translates to 0.3 mm s^{-1} in the measurements. However, it is to be noted this value of uncertainty is relevant only in case of measurements of r.m.s. velocity. The correlation maps and the PDFs have much smaller residual r.m.s. error due to the process of averaging. The systematic peak-locking error, typically of a magnitude of 0.02 px, is far larger than the residual random errors. However, the peak-locking error is also corrected (see figure 20). Additional details can be found in Cholemari (2007).

However, the technique of PIV itself would incur errors such as filtering effect of a limited spatial resolution, behaviour of tracer particles in following the flow and non-uniformity of optics. We ensured that the optical irregularities were minimal by recording a grid of 1 mm^2 square pattern, placed within the setup with the fluids present. Even near the edges of the image, the irregularities could not be detected within a pixel. Further, the free fall velocity of the particles was 26 μm s^{-1}, about two orders of magnitude smaller than the average r.m.s. velocities. We discuss the effects of the limitation of the spatial resolution below and ensure that the effects are not significant for the present purposes by comparing statistics from measurements at two different resolutions.

The effect of the spatial resolution on turbulence statistics varies depending on the variable considered (Saarenrinne & Piirto 2000; Saarenrinne, Piirto & Eloranta 2001). Saarenrinne *et al.* (2001) assume that filtering eliminates 'all' the energy below the resolved scale. By looking at typical turbulence spectra, they conclude that the r.m.s. velocities are resolved to within 5% when $\Delta/\eta \sim 20$. In synthetic PIV images of Lecordier *et al.* (2001), the error is about 7% for $\Delta/\eta \sim 11$. In case of Hyun *et al.* (2003), for $\Delta/\eta \sim 25$, the error is about 15%, even in a high-shear zone. In our case the main measurements are with $\Delta/\eta \sim 4$, and the fine measurements are with $\Delta/\eta \sim 2$, and hence we can assume that the r.m.s. values are resolved to better than 5%.

When we consider the PDFs, we are looking at individual measurements and not averages. (Although, after binning, the PDFs of various data sets themselves are averaged.) Each of the measurements is potentially underestimated by the filtering

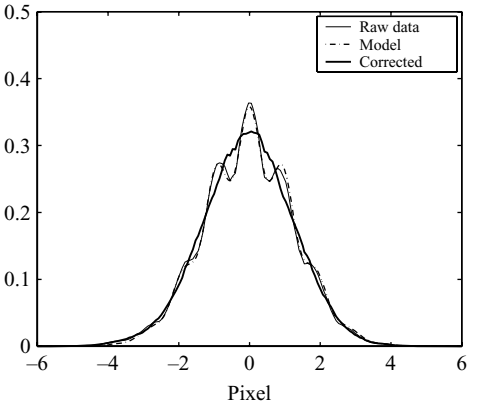

FIGURE 20. Correction of peak-locking errors. Data are a set of 250 velocity frames, from set a (resolution $\Delta/\eta = 4$). The amplitude of correction is 0.023 px. The model error used to correct the data is also shown.

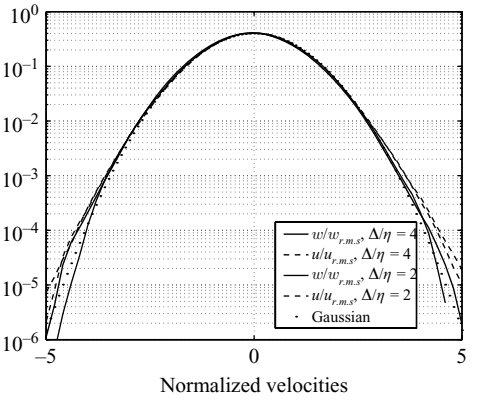

FIGURE 21. Comparison of velocity PDFs for set a and set b. The zoomed experiment data are shown using thin lines. The dots are the Gaussian curve.

of the small scales. Since the velocities at the small scales are small compared to the energy-containing scales, similar errors accrue as in the case of r.m.s. measurements. However, it could happen that, locally and instantaneously, the small scales have large velocities, and if the resolution is insufficient, these might not be resolved. We cannot determine this effect *a priori*, but by comparing the PDFs of the velocity differences (see figure 22) at the small separations (focusing on the small scales) of $\delta/\eta \sim 4$ and $\delta/\eta \sim 8$, we see that there is no significant difference between the measurements at a resolution of $\Delta/\eta \sim 4$ and the finer resolution measurements at $\Delta/\eta \sim 2$. And we conclude that errors due the spatial resolution in the PDF measurements are not significant.

Errors in the mean values and the correlations due to the filtering effect are again similar to those in case of the r.m.s.

Saarenrinne & Piirto (2000) estimated that the error in the measurement of dissipation ϵ is about 10% at $\Delta/\eta \sim 2$ and about 35% at $\Delta/\eta \sim 7.5$. For our measurements (with $\Delta/\eta \sim 4$) this error is about 20%, and hence the gradients accrue an error of about 10%.

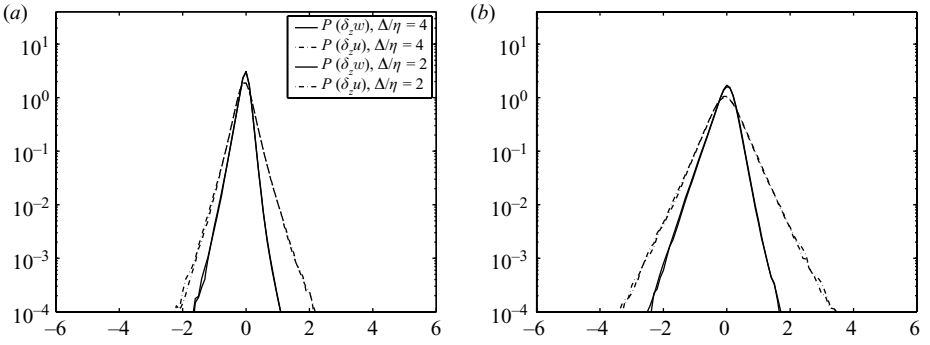

FIGURE 22. Comparison of the PDFs of velocity differences for resolutions $\Delta/\eta = 4$ and 2. Data from only the middle third of the pipe are considered. (*a*) $\Delta z/\eta = 4$; (*b*) $\Delta z/\eta = 8$.

Figure 19 shows the profiles of the r.m.s. values of the axial and lateral velocities for set a. Also shown using thin lines are the corresponding values for set b. We ensured that the r.m.s. data for set a had converged. However, for set b they have not converged but are within 5% of the converged profiles. The large number of frames are required because of the large correlation times (around 10 s), and hence large scales (corresponding to the large time scales) require more number of frames. Further, as seen in figure 11, the lateral extent of the correlated region of the axial velocity is less than, and the axial extent of correlation is more than, those of lateral velocity (thus less number of independent data points when averaged axially and hence requires a larger data set). Convergence for u_{rms} profile from set b in figure 19 is much better compared to that for the w_{rms} profile. Figure 20 shows a velocity histogram for a 250 s period, before and after correction for peak locking, showing the peak locking is corrected well. It is to be noted that the magnitude of the correction was only about 0.02 px, but the systematic error causes a large effect on the PDFs (Christensen 2004). Also, the symmetry at small values shows that the particle buoyancy does not significantly affect the measurements. Figure 21 shows the PDFs of velocity for data sets a and b. It is seen that the PDFs agree well at small velocities, though the agreement becomes poorer at larger velocities. However, in figure 22, the PDFs of velocity differences again agree very well. This is because the data corresponding to large scales (and large velocities) have not yet converged (see figure 19) for the zoomed data, but the data for velocity differences at smaller scales in figure 22 have converged. We judged the deviation between the zoomed and the whole pipe data in figures 19 and 21 was due to lack of convergence at the large scales in the zoomed data.

We thus conclude that, for the purposes of this study, the PIV implementation is adequate.

Appendix B. Axial homogeneity

If the pipe is long enough, away from the ends of the pipe the flow is expected to be axially homogeneous or fully developed, with the statistics of the flow and in particular the various averages having no dependence on z, the axial coordinate. An analogous axially homogeneous situation is obtained in a fully developed pressure-driven pipe flow. We now show these factors imply a linear variation in the axial (z) direction of the mean concentration. Further the mean concentration C can be shown

to be a constant across the cross-section of the pipe. We assume that the flow is fully developed; the mean flow is zero; and the Reynolds shear stresses are zero.

With the quasi-stationary assumption the mean scalar balance is

$$\alpha \partial_j^2 C - \partial_j \langle u_j c \rangle = 0, \tag{B 1}$$

where α is the salt diffusivity; $\tilde{c} = C + c$ is the salt concentration $(\rho - \rho_0)/\beta\rho_0$ with ρ_0 being the density of water. Capitalized variables and angular brackets indicate the ensemble means, and the lower case letters indicate the fluctuations from the mean. The mean velocities U_i are zero, and no assumption need be made on the full development of concentration C.

Applying the divergence theorem to (B 1) and noting that the velocities and the wall normal gradients of concentration are zero at the walls, we get

$$\int_A (-\alpha \partial_z^2 C + \partial_z \langle wc \rangle) \mathrm{d}A = 0, \tag{B 2}$$

and since full development implies $\partial_z \langle wc \rangle = 0$, we get $\int_A \partial_z^2 C \mathrm{d}A = 0$.

We will next show that $\langle \rho \rangle$ and thus C are constant across the cross-section. We consider the axial momentum equation in the fully developed region of the pipe. The axial momentum equation (with the Boussinesq approximation) is

$$\begin{aligned} \frac{\partial W}{\partial t} + U\frac{\partial W}{\partial x} + V\frac{\partial W}{\partial y} + W\frac{\partial W}{\partial z} &= -\frac{1}{\rho_0}\frac{\partial P}{\partial z} \\ &+ \nu \nabla^2 W - \frac{\partial \langle uw \rangle}{\partial x} - \frac{\partial \langle vw \rangle}{\partial y} - \frac{\partial \langle ww \rangle}{\partial z} - \frac{\rho^*}{\rho_0} g. \end{aligned} \tag{B 3}$$

With the quasi-steady and fully developed flow with no mean velocity ($\partial_z \langle \cdot \rangle = 0$, $U = 0$, $V = 0$ and $W = 0$), the left-hand side is zero. Because of full development $\partial_z \langle ww \rangle = 0$. The Reynolds shear stresses are zero: $\langle uw \rangle = 0$ and $\langle vw \rangle = 0$. Since the concentration profile is fully developed, we write $\rho^*(x, y, z) = \rho_A(z) + \delta\rho(x, y)$, where $\rho_A = 1/A_P \int_A \langle \rho \rangle dA$ is the average density over the pipe cross-section A_P. The deviation from the cross-section average $\delta\rho$ is just a function of (x, y) as is required by full development. (Note that this is an ensemble average value and not the turbulent density fluctuation.) Thus the axial momentum equation becomes

$$\left[-\frac{\partial P}{\partial z} - \rho_A g \right] - \delta\rho\, g = 0. \tag{B 4}$$

Consider the lateral momentum equations, the x equation, for example:

$$\frac{DU}{Dt} = 0 = -\frac{1}{\rho_0}\frac{\partial P}{\partial x} + \nu \nabla^2 U - \partial_x \langle uu \rangle - \partial_y \langle uv \rangle - \partial_z \langle uw \rangle. \tag{B 5}$$

Since U is zero, the advective and the viscous terms are zero; $\langle uv \rangle = 0$, as the flow is mean shear free, and $\partial_z \langle uw \rangle = 0$ because of full development (follows by the shear free nature of the flow as well). Thus $\partial P/\partial x = \rho_0 \partial_x \langle uu \rangle$. Integrating from the wall, we get

$$P = \rho_0 \langle uu \rangle + P_w(y, z), \tag{B 6}$$

where P_w is the pressure at the wall and is constant in x. Differentiating this with respect to z we get

$$\frac{\partial P}{\partial z} = \frac{\partial P_w(z, y)}{\partial z} + \rho_0 \partial_z \langle uu \rangle. \tag{B 7}$$

The last term is zero because of full development, and so $\partial P/\partial z$ is not a function of x – and by symmetry not a function of y as well. The terms in the square brackets in (B 4) are just functions of z and therefore must separately balance; $[-(1/\rho_0)(\partial P/\partial z)-\rho_A g]=0$. Therefore $\delta\rho=0$ (from (B 4)), and the mean concentration across the pipe is constant, $C=C(z)=\rho_A/(\beta\rho_0)$. From this and (B 2) $\partial_z C$ is seen to be constant; i.e. a fully developed flow implies the mean concentration varies linearly along z. Further, (B 4) implies that the mean pressure varies quadratically with z.

The existence of a linear concentration gradient was experimentally verified. An experiment was done using a pipe of 50 mm diameter and $AR=10$, with potassium permanganate at about 200 p.p.m. initially in the top tank, in addition to the salt. During the experiment, the pipe was illuminated from using an overhead projector and the light after passing through the flow was made to fall on a translucent screen. This image was recorded using a video camera and digitized. The difference in the intensity between an experimental image and a calibration image with no dye gives the amount of light absorbed due to the dye. We ensured, by means of a separate calibration, that the amount of light absorbed varied linearly with the dye concentration at the small concentrations involved. The average result of a number of frames over a couple of minutes, averaged across a region spanning about a third of the pipe cross-section near the axis of the pipe, was taken as the mean concentration in the pipe. The advantage of averaging is that not just the concentration fluctuations but also the ensuing refractive index variations get averaged out. Figure 3 shows the results of the experiments. It is seen that the concentration variation is fairly linear in the range measured, i.e. about two diameters from either end. From the plot we see that the number of data points is not sufficient for a converged concentration profile. Due to experimental constraints we could not measure the concentration profiles till the ends of the pipe. However, in the present flow, the developmental region at either end is short, about one diameter, much smaller compared to the case of pressure driven pipe flow (Cholemari & Arakeri (2005)).

REFERENCES

Amati, G., Koal, K., Massaioli, F., Sreenivasan, K. R. & Verzicco, R. 2005 Turbulent thermal convection at high Rayleigh numbers for a Boussinesq fluid of constant Prandtl number. *Phys. Fluids* **17** (121701), 1–4.

Arakeri, J. H., Avila, F. E., Dada, J. M. & Tovar, R. O. 2000 Convection in a long vertical tube due to unstable stratification-a new type of turbulent flow? *Curr. Sci.* **79** (6), 859–866.

Arakeri, J. H. & Cholemari, M. R. 2002 Fully developed buoyancy driven turbulence in a tube. In *Proc. Ninth Asian Cong. Fluid Mech.* (ed. E. Shirani & A. R. Pishevar). Isfahan University of Technology, Iran.

Aronson, D. Johansson, A. V. & Löfdahl, L. 1997 Shear free turbulence near a wall. *J. Fluid Mech.* **338**, 363–385.

Batchelor, G. K., Canuto, V. M. & Chasnov, J. R. 1991 Homogeneous buoyancy-generated turbulence. *J. Fluid Mech.* **235**, 349–378.

Calzavarini, E., Lohse, D., Toschi, F. & Tripiccione, R. 2005 Rayleigh and prandtl number scaling in the bulk of rayleigh-bnard turbulence. *Phys. Fluids* **17** (055107), 1–7.

Chandrasekhar, S. 1981 *Hydrodynamic and Hydromagnetic Stability*. Dover Publications.

Cholemari, M. R. 2004 Buoyancy driven turbulence in a vertical pipe. PhD thesis. Department of mechanical engineering, Indian Institute of Science, Bangalore, Karnataka, India.

Cholemari, M. R. 2007 Modelling and correction of peak-locking in digital PIV. *Exp. Fluids* **42** (6), 913–922.

Cholemari, M. R. & Arakeri, J. H. 2005 Experiments and a model of turbulent exchange flow in a vertical pipe. *Int. J. Heat Mass Transfer* **48**, 4467–4473.

Cholemari, M. R. & Arakeri, J. H. 2006 A model relating eulerian spatial and temporal velocity correlations. *J. Fluid Mech.* **551**, 19–29.

Christensen, K. T. 2004 On the influence of peaklocking errors on turbulence statistics compared from PIV ensembles. *Exp. Fluids* **36** (3), 484–497.

Constantin, P. & Doering, C. R. 1999 Infinite prandtl number convection. *J. Stat. Phys.* **94** (1–2), 159–172.

Debacq, M., Fanguet, V., Hulin, J.-P., Salin, D. & Perrin, B. 2001 Self-similar concentration profiles in buoyant mixing of miscible fluids in a vertical tube. *Phys. Fluids* **13**, 3097.

Debacq, M., Hulin, J.-P. & Salin, D. 2003 Buoyant mixing of miscible fluids of varying viscosities in vertical tubes. *Phys. Fluids* **15** (12), 3846–3855.

Doering, C. R., Otto, F. & Reznikoff, M. G. 2006 Bounds on vertical heat transport for infinite-Prandtl-number Rayleigh–Benard convection. *J. Fluid Mech.* **560**, 229–241.

Epstein, M. 1988 Buoyancy driven exchange flow through small openings in horizontal partitions. *J. Heat Transfer* **110**, 885–893.

Fitzjarrald, D. E. 1976 An experimental study of turbulent convection in air. *J. Fluid Mech.* **73** (pt. 4), 693–719.

Gardener, G. C. 1977 Motion of miscible and immiscible fluids in closed horizontal and vertical ducts. *Int. J. Multiphase Flow* **3**, 305–318.

Gibert, M., Pabiou, H., Chilla, F. & Castaing, B. 2006 High-Rayleigh-number convection in a vertical channel. *Phys. Rev. Lett.* **96**, 084501-1–084501-4.

Grossmann, S. & Lohse, D. 2000 Scaling in thermal convection: a unifying theory. *J. Fluid Mech.* **407**, 27–56.

Hunt, J. C. R. & Graham, J. M. R. 1978 Free stream turbulence near plane boundaries. *J. Fluid Mech.* **84**, 209–235.

Hyun, B. S., Balachander, R., Yu, K. & Patel, V. C. 2003 Assessment of PIV to measure mean velocity and turbulence in open channel flow. *Exp. Fluids* **35**, 262–267.

Keane, R. D. & Adrian, R. J. 1992 Theory of cross-correlation analysis of PIV images. *Appl. Sci. Res.* **49**, 191–215.

Kim, J. Moin, P. & Moser, R. D. 1987 Turbulence statistics in fully developed channel flow at low Reynolds number. *J. Fluid Mech.* **177**, 133–166.

Kraichnan, R. H. 1962 Turbulent thermal convection at arbitrary prandtl number. *Phys. Fluids* **5** (11), 1374–1389.

Lecordier, B., Demare, D., Vervisch, L. M. J., Réveillon, J. & Trinité, M. 2001 Estimation of the accuracy of PIV treatments for turbulent flow studies by direct numerical simulation of multi-phase flow. *Meas. Sci. Technol.* **12** (1382–1391).

Lohse, D. & Toschi, F. 2003 Ultimate state of thermal convection. *Phys. Rev. Lett.* **90** (3), 034502.

Monin, A. S. & Yaglom, A. M. 1971 *Statistical Fluid Mechanics: Mechanics of Turbulence* (vol. 1). The MIT press.

Niemela, J. J., Skrbek, L., Sreenivasan, K. R. & Donnelly, R. J. 2000 Turbulent convection at high Rayleigh numbers. *Nature* **404**, 837–841.

Niemela, J. J., Skrbek, L., Sreenivasan, K. R. & Donnelly, R. J. 2001 The wind in confined thermal convection. *J. Fluid Mech.* **449**, 169–178.

Niemela, J. J. & Sreenivasan, K. R. 2003 Confined turbulent convection. *J. Fluid Mech.* **481**, 355–384.

Niemela, J. J. & Sreenivasan, K. R. 2006 Turbulent convection at high Rayleigh numbers and aspect ratio 4. *J. Fluid Mech.* **557**, 411–422.

Nikolaenko, A., Brown, E., Funfschilling, D. & Ahlers, G. 2005 Heat transport by turbulent Rayleigh-Bénard convection in cylindrical cells with aspect ratio one and less. *J. Fluid Mech.* **523**, 251–260.

Noullez, A., Wallace, G., Lempert, W., Miles, R. B. & Frisch, U. 1997 Transverse velocity increments in turbulent flow using the relief technique. *J. Fluid Mech.* **339**, 287–307.

Perot, B. & Moin, P. 1995 Shear free turbulent boundary layers. Part 1. Physical insights to near wall turbulence. *J. Fluid Mech.* **295**, 199–227.

Pope, Stephen B. 2000 *Turbulent Flows*. Cambridge University Press.

Prasad, A. K. 2000 Particle image velocimetry. *Curr. Sci.* **79**, 51–60.

Raffel, M., Willert, C. E. & Kompenhans, J. 1998 *Particle Image Velocimetry*. Springer.

Roche, P.-E., Castaing, B., Chabaud, B. & Hébral, B. 2001 Observation of the 1/2 power law in Rayleigh–Bénard convection. *Phys. Rev.* E **63**, 045303.

Saarenrinne, P. & Piirto, M. 2000 Turbulent kinetic energy dissipation rate estimation from PIV velocity vector fields. *Exp. Fluids* (suppl.) **29** (7), S300–S307.

Saarenrinne, P., Piirto, M. & Eloranta, H. 2001 Experiences of turbulence measurement with PIV. *Meas. Sci. Technol.* **12**, 1904–1910.

Siggia, E. D. 1994 High Rayleigh number convection. *Annu. Rev. Fluid Mech.* **26**, 137–168.

Stringano, G. & Verzicco, R. 2006 Mean flow structure in thermal convection in a cylindrical cell of aspect ratio one half. *J. Fluid Mech.* **548**, 1–16.

Tennekes, H. & Lumley, J. L. 1972 *A First Course in Turbulence*. The MIT press.

Theerthan, S. A. & Arakeri, J. H. 1998 A model for near-wall dynamics in turbulent Rayleigh–Bénard convection. *J. Fluid Mech.* **373**, 221–254.

Theerthan, S. A. & Arakeri, J. H. 2000 Planform structure and heat transfer in turbulent free convection over horizontal surfaces. *Phys. Fluids* **12** (4), 884–894.

Thomas, N. H. & Hancock, P. E. 1977 Grid turbulence near a moving wall. *J. Fluid Mech.* **82**, 481–496.

Uzkan, T. & Reynolds, W. C. 1967 A shear-free turbulent boundary layer. *J. Fluid Mech.* **28**, 803–821.

Verzicco, R. & Sreenivasan, K. R. 2008 Confined thermal convection in a 'cigar box' cylindrical cell. Private communication.

Westerweel, J. 1997 Fundamentals of digital particle image velocimetry. *Meas. Sci. Technol.* **8**, 1379–1392.

Westerweel, J., Dabiri, D. & Gharib, M. 1997 the effect of a descrete window offset on the accuracy of cross-correlation analysis of digital PIV recordings. *Exp. Fluids* **23**, 20–28.